BAR scaffolds drive membrane fission by crowding disordered domains

Wilton T. Snead [a], Wade F. Zeno [a], Grace Kago [a], Ryan W. Perkins [a], J Blair Richter [b], Eileen M. Lafer [b], Jeanne C. Stachowiak [a,c,1]

Affiliations

[a] Department of Biomedical Engineering, The University of Texas at Austin, Austin, TX, 78712, USA; [b] Department of Biochemistry and Structural Biology, Center for Biomedical Neuroscience, The University of Texas Health Science Center at San Antonio, San Antonio, TX, 78212, USA; [c] Institute for Cellular and Molecular Biology, The University of Texas at Austin, Austin, TX, 78712, USA

[1] To whom correspondence should be addressed:
Jeanne C. Stachowiak (jcstach@austin.utexas.edu).

Abstract

Cellular membranes are remodeled continuously to facilitate membrane traffic, organelle biogenesis, and cell division. The crescent-shaped bin-amphiphysin-rvs (BAR) domains are a key class of membrane remodeling proteins, which polymerize into ordered cylindrical scaffolds that transform membranes into tubules. Isolated BAR domains stabilize these tubules against membrane fission, the division of membrane surfaces into separate compartments. But in nature BAR domains are rarely isolated. Instead they are part of multi-domain proteins that frequently contain intrinsically-disordered regions of substantial molecular weight. How might these bulky disordered regions alter the membrane shaping functions of BAR domains? Here we show that full-length amphiphysin and FCHo1 proteins, which respectively contain highly-curved N-BAR and modestly-curved F-BAR domains coupled to large disordered regions, are surprisingly potent drivers of membrane fission. Specifically, we use multiple, independent assays to demonstrate that when these BAR scaffolds assemble at membrane surfaces, their bulky disordered domains become highly concentrated, generating substantial steric pressure that destabilizes tubules, promoting fission. These findings illustrate a mechanism that overcomes the energetic barrier to membrane fission by coupling structure-driven membrane scaffolding to entropically-driven protein crowding. Interestingly, this behavior applies to BAR domains with a range of curvatures, suggesting that the ability of BAR scaffolds to concentrate disordered domains, rather than their inherent structural curvature, is the key requirement for fission. More broadly, this work challenges the paradigm that BAR domain-containing proteins stabilize membrane tubules, suggesting instead that they are key components of the membrane fission machinery.

Introduction

Cellular membranes must undergo dynamic remodeling to facilitate essential cellular processes including formation of trafficking vesicles[1], viral egress[2], and cytokinesis[3]. Since membranes resist deformation[4], cells employ specialized protein machines to drive membrane remodeling[5]. For example, the crescent-shaped, dimeric bin-amphiphysin-rvs (BAR) domains[6-8] polymerize into cylindrical scaffolds on membrane surfaces, forcing the underlying membrane to adopt the tubular geometry of the scaffold[9]. This rigid scaffold is thought to stabilize membrane tubules, preventing division into separate membrane compartments through the process of membrane fission[10].

Importantly, a large number of studies on the membrane shaping behavior of BAR domains in vitro have examined the BAR domain in isolation, with significant portions of the protein removed. Examples include the N-terminal amphipathic helix BAR (N-BAR) domain of amphiphysin[11], the FCH BAR (F-BAR) domain of FCHo1/2[12, 13], the F-BAR domain of the neuronal migration protein srGAP2[14], the F-BAR domains of the cytokinesis proteins Imp2[15] and Cdc15[16], and the inverted BAR (I-BAR) domains of MIM and ABBA[17, 18], among others. However, these BAR domains do not exist in isolation in the cell, but rather as part of large, multi-domain proteins which frequently contain long, intrinsically-disordered protein (IDP) domains[13, 19-22]. How do these IDP domains influence the membrane remodeling behavior of BAR domains?

Recent work from our lab[23, 24] and others[25-29] has revealed that molecular crowding among proteins attached to membrane surfaces at high density generates steric pressure, which provides a potent force for membrane shaping. Further, previous work found that IDP domains, which occupy large footprints on the membrane surface in comparison to well-folded proteins of equal molecular weight[30], enhanced the efficiency of membrane bending and fission[31, 32]. However, a fundamental question has remained unanswered, limiting the potential of protein crowding to explain membrane remodeling in cells. What brings bulky domains together to generate steric pressure? In particular, what keeps crowded proteins from simply diffusing away from one another, dissipating steric pressure and inhibiting membrane shaping? Proteins such as amphiphysin[11, 19] and FCHo1/2[12, 13], which contain both scaffold-forming BAR domains and bulky disordered domains, present a possible solution to this problem. Specifically, the ability of BAR domains to form scaffolds has the potential to locally concentrate disordered domains such that steric pressure is amplified rather than dissipated.

Here we set out to investigate the impact of disordered domains on the membrane remodeling ability of BAR proteins. To our surprise, we found that while isolated BAR domains formed stable membrane tubules, full-length amphiphysin and FCHo1 destabilized these tubules, leading to highly efficient membrane fission. Our results

directly challenge the paradigm that BAR scaffolds stabilize membrane tubes, and suggest instead that these scaffolds act as templates that locally enhance steric pressure, driving fission through protein crowding.

Results and Discussion

While the amphiphysin N-BAR domain stabilizes membrane tubules, full-length amphiphysin drives membrane fission.

Amphiphysin is composed of an N-terminal, amphipathic helix BAR (N-BAR) domain, followed by an intrinsically disordered protein (IDP) domain of approximately 383 amino acids in humans, and a C-terminal SH3 domain[11, 19, 33, 34] (Fig. 1a). To compare membrane bending by full-length amphiphysin (Amph-FL) to the N-BAR domain alone, we first examined the effects of each protein on giant unilamellar vesicles (GUVs). These experiments revealed that both the N-BAR domain and Amph-FL drove potent membrane bending, forming mobile, diffraction-limited tubules that extended from the GUV surface (Fig. 1b and Supplementary Videos 1 and 2). These GUVs often collapsed or broke apart into smaller tubules and fragments (Supplementary Videos 3 and 4), suggesting that tubulation may not have been the endpoint of the membrane remodeling process. In order to directly visualize the morphology of these membranes at the end of remodeling, we utilized negative stain transmission electron microscopy (TEM) to resolve membrane structures below the optical diffraction limit.

As expected from previous findings[11, 35], the N-BAR domain efficiently transformed vesicles that had an average initial diameter of 200 nm into long tubules with average outer diameter 44±6 nm s.d. (Fig. 1c,d and Supplementary Fig. S1a,b). In contrast, Amph-FL did not drive appreciable membrane tubulation in TEM experiments. Rather, Amph-FL divided the vesicles of initially 200 nm diameter into a population of highly curved vesicles with a peak diameter centered near 22 nm (Fig. 1e,f and Supplementary Fig. S1c). This result suggests that Amph-FL is capable of driving membrane fission, a more energetically demanding process than membrane tubulation[36]. To confirm and better understand the ability of amphiphysin to drive membrane fission, we compared N-BAR and Amph-FL in two additional assays of membrane fission.

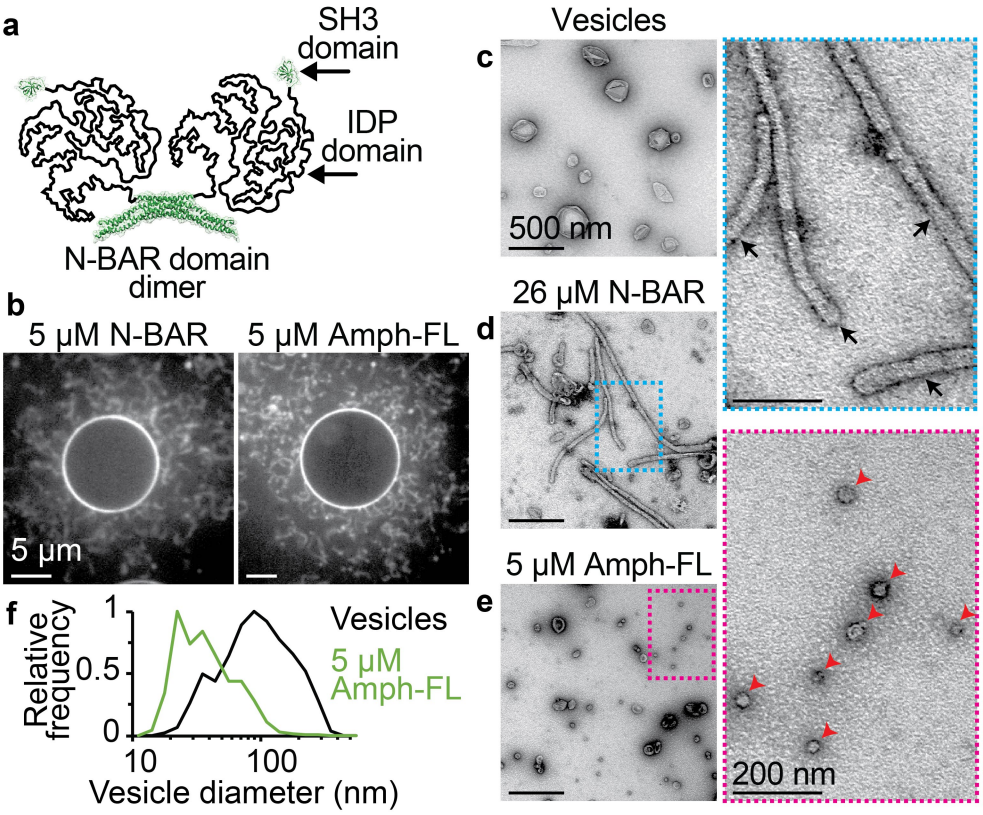

Figure 1. Amphiphysin drives membrane fission, while the N-BAR domain stabilizes membrane tubules. GUV membrane composition: 79.5 mol% DOPC, 5 mol% PtdIns(4,5)P_2, 15 mol% DOPS, 0.5 mol% Oregon Green 488-DHPE. Membrane composition for vesicles in TEM: 80 mol% DOPC, 5 mol% PtdIns(4,5)P_2, 15 mol% DOPS. (**a**) Schematic of full-length amphiphysin (Amph-FL) dimer. BAR domain: PDB 4ATM. SH3 domain: PDB 1BB9. (**b**) Representative spinning disc confocal micrographs of GUVs after exposure to 5 μM of either N-BAR or Amph-FL. Fluorescence signal comes from Atto 594-labeled protein. (**c-e**) Negative stain TEM micrographs of 200 nm extruded vesicles (**c**) before exposure to protein, (**d**) after exposure to 26 μM N-BAR, and (**e**) after exposure to 5 μM Amph-FL. Dashed boxes indicate zoomed regions to the right. Black arrows indicate membrane tubules, red arrowheads indicate fission vesicles. (**f**) Histograms of vesicle diameters measured from electron micrographs. Amph-FL generates a high-curvature vesicle population with a peak centered near 22 nm diameter not observed before protein exposure. Vesicles alone: n = 1,302 vesicles. 5 μM Amph-FL: n = 1,071 vesicles. Scale bars (b): 5 μm. Scale bars in (c-e): 500 nm. Zoomed region scale bars: 200 nm.

Full-length amphiphysin generates highly curved fission products.

To further quantify membrane fission, we used supported bilayers with extra membrane reservoir (SUPER templates), which are glass beads surrounded by a low-tension membrane. Exposure of SUPER templates to fission-driving proteins results in measurable membrane release from the beads[37-39]. SUPER template experiments revealed that while both N-BAR and Amph-FL drove membrane release in the

concentration range of 50-1,000 nM, Amph-FL drove more than twice as much (2.6 to 4.7-fold greater) membrane release at each concentration (Fig. 2a). Notably, membrane release does not directly imply membrane fission, as both vesicles and lipid tubules can be shed from SUPER templates.

We next employed a tethered vesicle assay to quantify the distributions of fission vesicle diameters over a range of protein concentrations[32]. Specifically, we tethered fluorescent vesicles to a coverslip passivated with PEG and PEG-biotin (Fig. 2b). Vesicles in these experiments contained a biotinylated lipid, which facilitated tethering to the substrate via binding to neutravidin. Vesicles also contained the fluorescent lipid Oregon Green 488-DHPE, which we used to quantify the brightness of each vesicle after imaging in confocal fluorescence microscopy (Fig. 2c). We then converted the resulting distributions of vesicle brightness to distributions of vesicle diameter by calibrating against the initial vesicle diameter distribution measured using dynamic light scattering (see methods).

Using this assay, we found that Amph-FL in the concentration range of 50-150 nM transformed vesicles with an average initial diameter of 200 nm (Fig. 2c,d) to a population of high curvature fission products (Fig. 2c,e) with average diameter 27±1 nm s.e.m. at 150 nM, in agreement with results from TEM (see Fig. 1e,f). The proportion of vesicles with diameters below 30 nm increased with increasing protein concentration, from less than 1% at 50 nM to approximately 45% at 150nM (Fig. 2g). In contrast, the N-BAR domain did not drive fission, even at higher protein concentrations (Fig. 2c, f, and g). Taken together, our results from electron microscopy and tethered vesicle experiments confirm that Amph-FL is a potent driver of membrane fission, while the isolated N-BAR domain is only capable of membrane tubulation.

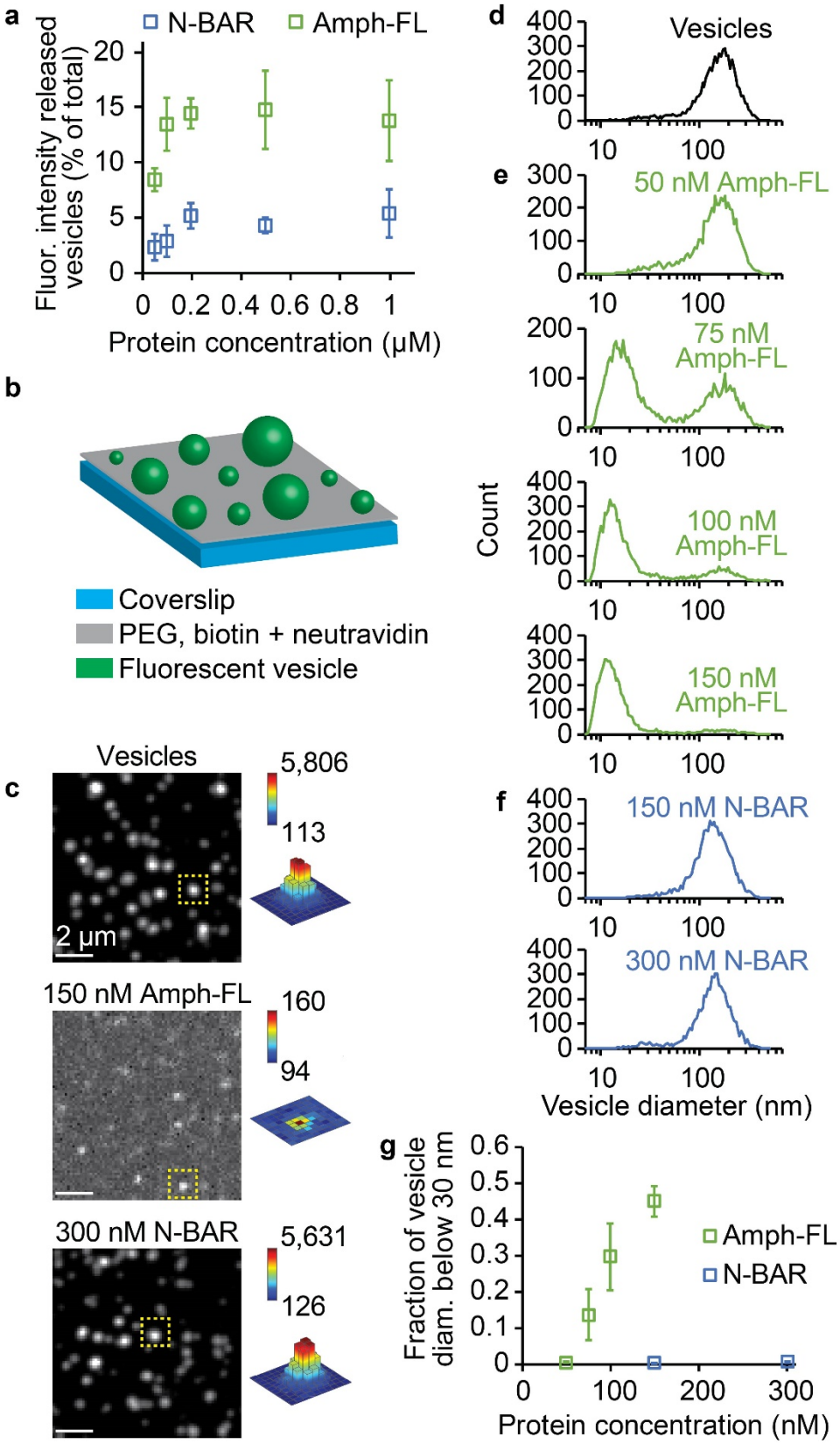
a
N-BAR
Amph-FL
Fluor. intensity released vesicles (% of total)
Protein concentration (μM)
b
Coverslip
PEG, biotin + neutravidin
Fluorescent vesicle
c
Vesicles
5,806
113
2 μm
150 nM Amph-FL
160
94
300 nM N-BAR
5,631
126
d
Vesicles
e
50 nM Amph-FL
75 nM Amph-FL
100 nM Amph-FL
150 nM Amph-FL
Count
f
150 nM N-BAR
300 nM N-BAR
Vesicle diameter (nm)
g
Fraction of vesicle diam. below 30 nm
Amph-FL
N-BAR
Protein concentration (nM)

Figure 2. Full-length amphiphysin produces highly curved fission products. SUPER template membrane composition: 79 mol% DOPC, 5 mol% PtdIns(4,5)P_2, 15 mol% DOPS, 1 mol% Texas Red-DHPE. Tethered vesicle composition: 76 mol% DOPC, 5 mol% PtdIns(4,5)P_2, 15 mol% DOPS, 2 mol% Oregon Green 488-DHPE, 2 mol% DP-EG10-biotin. (**a**) Membrane release from SUPER templates was measured as Texas Red signal present in the supernatant after sedimentation of the SUPER templates. Membrane release in the absence of protein was measured and subtracted as background. (**b**) Schematic of tethered vesicle fission experiment. (**c**) Representative spinning disc confocal micrographs of tethered vesicles before exposure to protein (top), after exposure to 150 nM Amph-FL (middle), and after exposure to 300 nM N-BAR (bottom). Contrast settings in top and bottom images are the same while contrast in middle image is adjusted to clearly show vesicle puncta. Dashed yellow boxes indicate puncta intensity profiles on right, where bar heights are all scaled between 90 and 6,000 brightness units while each color map corresponds to specified intensity range. (**d-f**) Distributions of vesicle diameter measured by tethered vesicle assay (**d**) before exposure to protein, (**e**) after exposure to Amph-FL at 50, 75, 100, and 150 nM, and (**f**) after exposure to N-BAR at 150 and 300 nM. (**g**) Summary of tethered vesicle fission data, expressed as the ratio of the distribution area below 30 nm diameter to the total distribution area. Scale bars in (c): 2 μm. Markers in (a) and (g) represent average ± first s.d., n = 3 independent experiments.

The ability of full-length amphiphysin to drive membrane fission does not arise from greater membrane binding affinity in comparison to isolated N-BAR.

How can we explain the ability of full-length amphiphysin to drive membrane fission? One possible explanation could be that the full-length protein may bind more strongly to membrane surfaces compared to the N-BAR domain alone, resulting in more potent membrane remodeling. To examine this possibility, we utilized a tethered vesicle assay similar to the experiments described above to quantify the relative extent of protein-membrane binding. In this assay proteins were labeled with Atto 594 dye, while vesicles contained the lipid Oregon Green 488-DHPE. We quantified vesicle diameter as described above, and used measurements of single fluorophore brightness to quantify the number of bound proteins per vesicle[32] (see methods). From these measurements we determined the density of membrane-bound proteins, which increased with increasing protein concentration in solution (Supplementary Fig. S2a-c). These experiments revealed that Amph-FL and N-BAR reached similar number densities of membrane-bound protein within the concentration range of 5-25 nM, indicating that Amph-FL and the isolated N-BAR domain bind with similar affinity to membranes (Supplementary Fig. S2d,e). Specifically, these results suggest that the IDP domain did not significantly enhance protein-lipid and protein-protein interactions, either of which would be expected to increase the density of membrane-bound protein. Therefore, the ability of Amph-FL to drive membrane fission cannot be explained by differences in membrane binding.

The disordered domain of amphiphysin drives membrane fission on its own, but requires higher protein concentration compared to full-length amphiphysin.

Another possible explanation for the ability of amphiphysin to drive membrane fission is that its substantial disordered domain (residues 240-622) generates steric pressure that promotes fission, in line with previous studies on other membrane-bound disordered domains[31, 32]. If so, the isolated disordered domain should be able to drive membrane fission when bound to membrane surfaces at sufficient density. To test this idea, we purified the disordered domain of amphiphysin, lacking the C-terminal SH3 domain (Amph CTD ΔSH3). This construct included an N-terminal hexa-histidine (6his) tag to facilitate binding to membranes by the lipid DOGS-NTA-Ni (Fig. 3a and Supplementary Fig. S3). Tethered vesicle fission experiments revealed that Amph CTD ΔSH3 indeed drove the formation of highly curved fission products (Fig. 3b,c). However, 100-fold greater concentration of Amph CTD ΔSH3 in solution (10 μM) was required to generate fission products of similar curvature to those observed with Amph-FL (100 nM) (see Fig. 2e,g).

Membrane binding experiments with fluorescently-labeled Amph CTD ΔSH3 revealed that at 10 μM of protein in solution, the protein covered more than 40% of the membrane surface (Fig. 3d and Supplementary Fig. S4). At this coverage, steric pressure from protein crowding is expected to be sufficient to overcome the energetic barrier to membrane fission[32]. Therefore, the requirement for a high solution concentration of Amph CTD ΔSH3 reflects the conditions needed to promote crowded binding to the membrane surface. In contrast, the ability of Amph-FL to drive fission at much lower concentrations likely arises from polymerization of the BAR domain scaffold, which enables multivalent membrane binding[40, 41]. In line with this thinking, we found that 100 nM Amph-FL, a concentration which drove potent fission (Fig. 2e,g), covered more than 90% of the membrane surface (Supplementary Fig. S2f). This coverage is significantly higher than has been observed for non-assembling proteins[32, 42]. Collectively, these results suggest that the ability of amphiphysin to drive efficient membrane fission arises from a collaboration between its N-BAR domain and disordered domain.

A chimera consisting of N-BAR fused to an alternative disordered domain drives fission with similar efficiency to wild-type amphiphysin.

Experiments comparing membrane remodeling by Amph-FL and N-BAR imply that assembly of the N-BAR scaffold at the membrane surface facilitates local crowding of the bulky disordered domains in Amph-FL. This idea suggests that any bulky disordered domain that is brought to the membrane surface by a BAR scaffold should be capable of driving potent membrane fission. To test this prediction, we created a chimera consisting of the amphiphysin N-BAR domain fused to the C-terminal IDP domain of rat epsin1 (N-BAR-epsin CTD, Fig. 3e and Supplementary Fig. S3). Importantly, the disordered domain of epsin1 is similar in length to the IDP of amphiphysin (383 versus 432 amino acids,

respectively). Tethered vesicle fission experiments revealed that N-BAR-epsin CTD generated highly curved fission products from vesicles with an initial average diameter of 200 nm within a similar range of protein concentrations to Amph-FL (Fig. 3f, compare to Fig. 2e). Further, both N-BAR-epsin CTD and Amph-FL produced a strikingly similar fraction of fission products with diameters below 30 nm at equivalent concentrations in solution (Fig. 3g). Finally, SUPER template membrane shedding experiments revealed that in the concentration range of 50-1,000 nM, N-BAR-epsin CTD drove greater membrane release compared to the isolated N-BAR domain (Fig. 3h), similar to the results of SUPER template experiments comparing N-BAR and Amph-FL (see Fig. 2a). These findings illustrate the ability of N-BAR scaffolds to promote membrane fission by crowding arbitrary disordered domains at membrane surfaces.

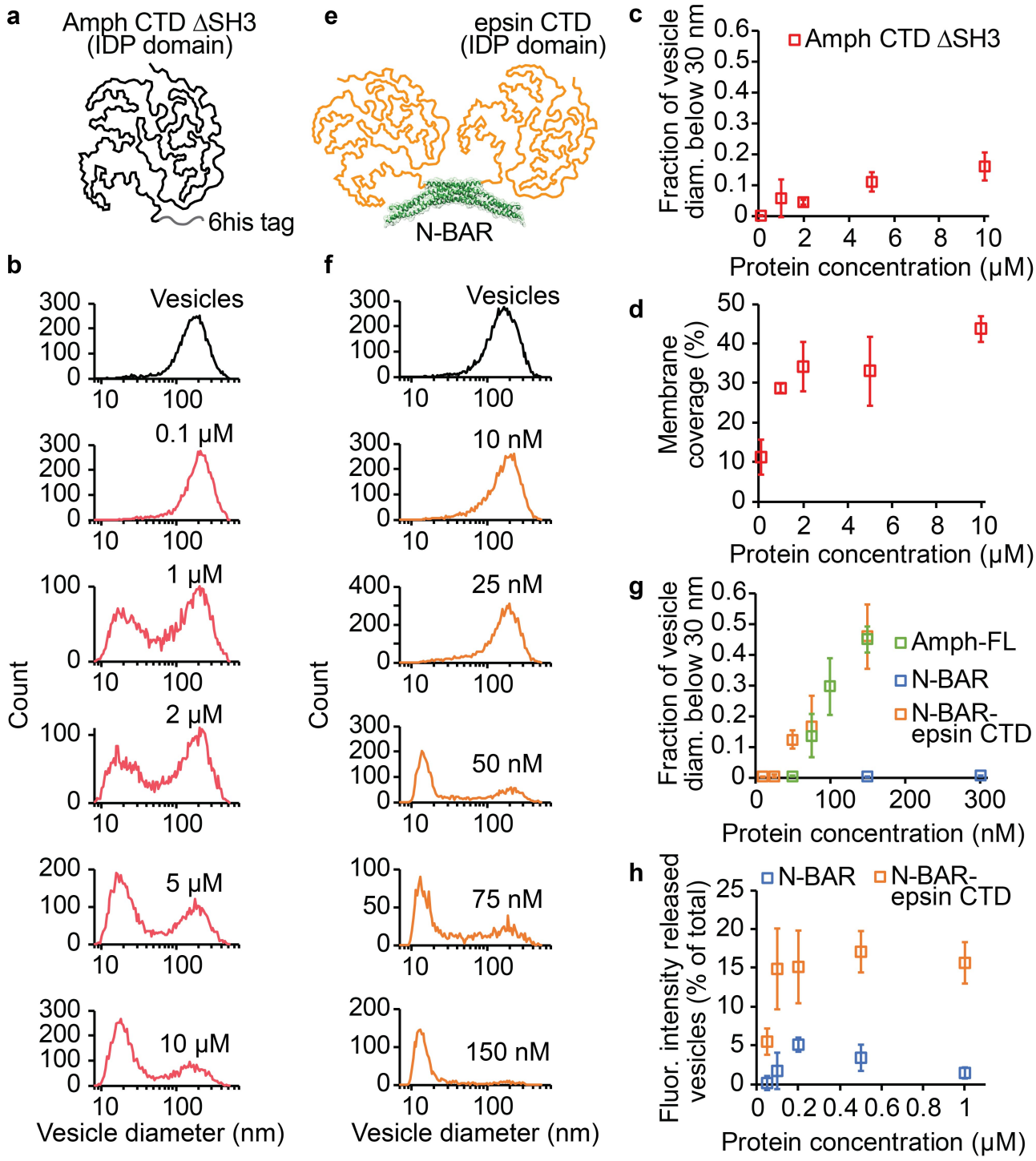

Figure 3. The disordered domain of amphiphysin alone drives membrane fission, but the N-BAR scaffold substantially enhances fission efficiency. Membrane composition in Amph CTD ΔSH3 tethered vesicle experiments: 76 mol% DOPC, 20 mol% DOGS-NTA-Ni, 2 mol% Oregon Green 488-DHPE, 2 mol% DP-EG10-biotin. In tethered vesicle experiments with N-BAR-epsin CTD, DOGS-NTA-Ni was replaced with 5 mol% PtdIns(4,5)P_2 and 15 mol% DOPS. SUPER template membrane composition: 79 mol% DOPC, 5 mol% PtdIns(4,5)P_2, 15 mol% DOPS, 1 mol% Texas Red-DHPE. (**a**) Schematic of Amph CTD ΔSH3. (**b**) Tethered

vesicle fission experiments show that Amph CTD ΔSH3 forms highly curved fission products. (**c**) Summary of data from tethered vesicle fission experiments with Amph CTD ΔSH3 expressed as the ratio of the distribution area below 30 nm to the total distribution area (compare to Fig. 2g). (**d**) Coverage of the membrane surface by Amph CTD ΔSH3 for each concentration at which fission was measured. (**e**) Schematic of N-BAR-epsin CTD chimera. (**f**) Tethered vesicle fission measurements show that N-BAR-epsin CTD generates highly curved fission vesicle populations over the concentration range of 10-150 nM, similar to Amph-FL (compare to Fig. 2e). (**g**) Summary of data from tethered vesicle fission experiments with N-BAR-epsin CTD, expressed as the ratio of the distribution area below 30 nm to the total distribution area. N-BAR-epsin CTD and Amph-FL follow a similar trend. Amph-FL and N-BAR data from Fig. 2g. (**h**) SUPER template experiments show that N-BAR-epsin CTD drives greater membrane release compared to N-BAR. Markers in (c), (d), (g), and (h) represent average ± first s.d., n = 3 independent experiments.

Crowding among disordered domains opposes the ability of I-BAR scaffolds to drive inward membrane bending.

We next asked how the membrane remodeling ability of crowded disordered domains compares with that of BAR scaffolds. To make this comparison, we created a chimeric protein that places the two mechanisms in direct competition within the same molecule. Specifically, we fused the I-BAR domain of human IRSp53 to the bulky, C-terminal IDP domain of rat AP180 (569 disordered amino acids) to form I-BAR-AP180 CTD (Fig. 4a). While the I-BAR domain is known to generate inverted membrane curvature[17, 18], the attached IDP should generate steric pressure that will tend to bend the membrane in the opposite direction. Exposing GUVs to the I-BAR domain alone drove inverted membrane tubulation, as expected (Fig. 4b, left and Supplementary Video 5). In contrast, the I-BAR-AP180 CTD chimera drove neither inward nor outward tubulation. Instead, the protein caused the GUV membrane to fluctuate dynamically through non-spherical shapes in which regions of gentle membrane curvature extending both inward and outward were apparent, (Fig. 4b, right and Supplementary Video 6). These “frustrated” fluctuations demonstrate that the disordered domain effectively neutralized the ability of the I-BAR domain to drive inward membrane bending. This result suggests that crowding among disordered domains and scaffolding by BAR domains make comparable contributions to membrane remodeling.

Membrane release experiments using SUPER templates showed that exposure to the I-BAR domain (100 nM - 5 μM) decreased the amount of membrane shedding to levels lower than the amount of non-specific shedding that occurred in protein-free buffer (Fig. 4c, negative values). This result suggests that assembly of the I-BAR scaffold stabilized the membrane against shedding. In contrast, I-BAR-AP180 CTD drove positive membrane release at all concentrations (Fig. 4c), demonstrating that the disordered domain of AP180 is capable of disrupting the membrane-stabilizing effect of I-BAR. Interestingly, tethered vesicle fission experiments revealed that the highest concentration

of I-BAR-AP180 CTD that we tested, 5 μM, drove membrane fission, generating a population of vesicles centered near 20 nm diameter (Fig. 4d). This result demonstrates that, under appropriate conditions, steric pressure among crowded IDPs is sufficient to overcome the structure-based curvature preference of the I-BAR scaffold. Importantly, while full-length IRSp53 does not contain a large IDP domain, the I-BAR domain-containing proteins MIM and ABBA do contain regions of substantial disorder (approximately 475 amino acids in MIM)[22]. Therefore, our observations raise the question of whether the presumed role of these proteins in driving inward cellular membrane protrusions can be justified on the basis of in vitro studies on their isolated I-BAR domains[17, 18].

An F-BAR scaffold drives fission by locally crowding bulky disordered domains.
If BAR scaffolds drive membrane fission by concentrating large disordered domains at membrane surfaces, then the ability of Amph-FL to drive fission (Fig. 1,2) should extend to other proteins that contain both BAR domains and substantial regions of intrinsic disorder. Interestingly, many proteins that contain the modestly curved F-BAR domain have this architecture[21], including the endocytic proteins FCHo1/2[13] and its yeast homolog Syp1[43], the srGAP proteins involved in neuronal development[20], and the cytokinesis proteins Cdc15[44] and Imp2[15] in *S. pombe* and Hof1[45] in *S. cerevisiae*. To test this idea, we examined FCHo1 (*C. elegans*), which consists of an N-terminal F-BAR domain followed by an intrinsically disordered domain of 412 amino acids and a C-terminal μ-homology domain[13, 46-48] (Fig. 4e). Negative stain TEM revealed that exposure of vesicles with an initial average diameter of 200 nm to the F-BAR domain of FCHo1 drove formation of lipid tubules with an average diameter of 21±2 nm s.d. (Fig. 4f,g and Supplementary Fig. S5a,b), in agreement with previous findings that the F-BAR domain can form high curvature tubules near 20 nm diameter[12, 13]. In contrast, full-length FCHo1 (FCHo1-FL) did not generate lipid tubules, but instead divided the 200 nm diameter vesicles into a population of highly curved vesicles with average diameter 17±7 nm s.d. (Fig. 4h and Supplementary Fig. S5c,d).

Similarly, tethered vesicle fission experiments revealed that FCHo1 drove potent membrane fission over the concentration range of 10-250 nM (Fig. 4i,k), a comparable range to Amph-FL (50-150 nM, Fig. 2e,g). However, the F-BAR domain alone did not drive fission in these experiments, even at substantially higher concentrations up to 2 μM (Fig. 4j,k). Interestingly, in these experiments, the fission products produced by FCHo1-FL had a peak diameter centered near 10 nm, a higher curvature than is normally associated with bilayer vesicles[49]. This finding suggests that FCHo1-FL may stabilize the formation of membrane micelles, which are similar in morphology to the hemifusion intermediates that form during membrane fission[36, 49]. Notably, vesicles in these experiments were composed primarily of the lipid DOPC, which has a lower bending

rigidity than physiological membranes[50]. In contrast, when we increased bilayer rigidity by replacing DOPC with a more rigid lipid, DPPC[50, 51], the average diameter of fission products increased to 30-40 nm, consistent with bilayer vesicles (Supplementary Fig. S6). Collectively, these studies show that F-BAR scaffolds are also capable of collaborating with IDP crowding to drive efficient membrane fission.

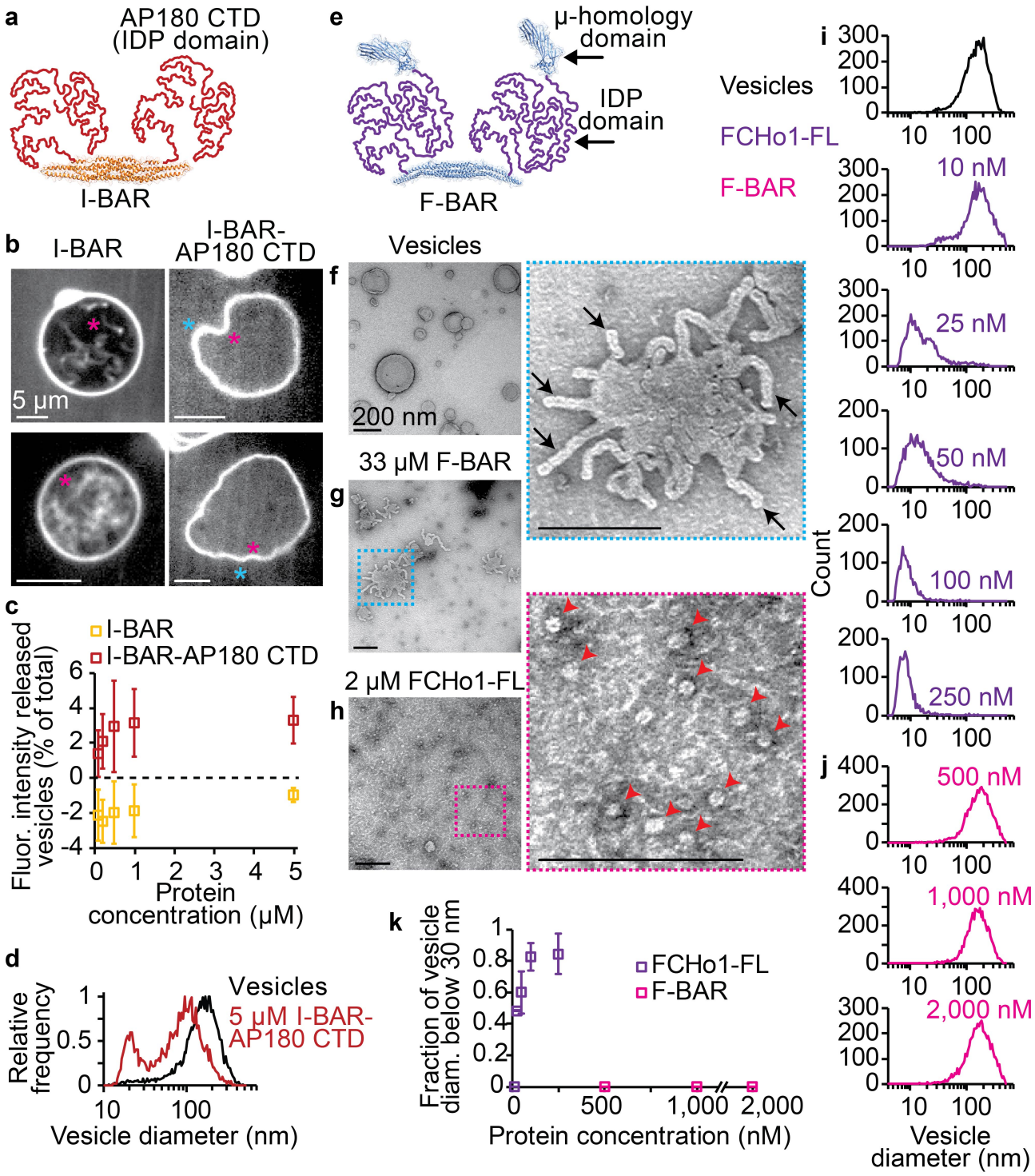

Figure 4. Disordered domain crowding opposes inverted membrane bending by I-BARs and promotes membrane fission by F-BARs. GUV membrane composition: 79.5 mol% DOPC, 5 mol% PtdIns(4,5)P_2, 15 mol% DOPS, 0.5 mol% Oregon Green 488-DHPE. SUPER template membrane composition: 79 mol% DOPC, 5 mol% PtdIns(4,5)P_2, 15 mol% DOPS, 1 mol% Texas Red-DHPE. Tethered vesicle membrane composition: 76 mol% DOPC, 5 mol% PtdIns(4,5)P_2, 15 mol% DOPS, 2 mol% Oregon Green 488-DHPE, 2 mol% DP-EG10-biotin. Membrane composition for vesicles in TEM: 80 mol% DOPC, 5 mol% PtdIns(4,5)P_2, 15 mol% DOPS. (**a**) Schematic of I-BAR-AP180 CTD chimera dimer. IRSp53 I-BAR domain: PDB 1Y2O. (**b**) Two representative confocal micrographs of GUVs after exposure to I-BAR or I-BAR-AP180 CTD. Asterisks indicate direction of membrane bending (magenta: inward; cyan: outward). Fluorescence signal comes from Atto 594-labeled protein. (**c**) SUPER template membrane release comparing I-BAR and I-BAR-AP180 CTD. (**d**) Tethered vesicle fission experiments reveal that 5 μM I-BAR-AP180 CTD generates highly curved fission vesicles. (**e**) Schematic of full-length FCHo1 (FCHo1-FL) dimer. F-BAR domain: PDB 2V0O. μ-homology domain: PDB 5JP2, chain A. (**f-h**) Negative stain TEM micrographs of 200 nm extruded vesicles (**f**) before exposure to protein, (**g**) after exposure to 33 μM F-BAR, and (**h**) after exposure to 2 μM FCHo1-FL. Dashed boxes indicate zoomed regions to the right. Black arrows indicate membrane tubules, red arrowheads indicate fission vesicles. (**i**) Tethered vesicle fission experiments reveal FCHo1-FL generates highly curved fission vesicles over the concentration range of 10-250 nM. (**j**) F-BAR does not drive fission in tethered vesicle fission experiments, even at concentrations up to 2,000 nM. (**k**) Plot of ratio of vesicle distribution area below 30 nm to the total distribution area (compare to Fig. 2g). Scale bars in (b): 5 μm. Scale bars in (f-h), including zoomed regions: 200 nm. Markers in (c) and (k) represent average ± first s.d., n = 3 independent experiments.

Here we report that membrane scaffolding by BAR domains works synergistically with steric pressure among bulky disordered domains to drive efficient membrane fission. By highlighting the ability of BAR scaffolds to locally concentrate IDP domains, this work helps to explain how steric pressure can be generated and sustained at membrane surfaces. Further, our findings are in direct contrast with the established view that BAR scaffolds prevent fission by stabilizing membrane tubes[10]. Instead, our work suggests that BAR proteins that contain substantial disordered regions should be re-classified as drivers of membrane fission. In support of this idea, work from the Drubin lab showed that the yeast amphiphysins Rvs161/167 are essential for membrane fission, and deletion of these proteins leads to a defect in the entry of clathrin-coated pits into cells[52, 53]. Depletion of amphiphysin by RNA interference also dramatically inhibits clathrin-mediated endocytosis in mammalian cells[54]. However, a similar endocytic defect is not observed when endophilin is depleted[54]. Endophilin contains an N-BAR domain and is recruited to late-stage clathrin-coated pits similar to amphiphysin, but does not contain a large IDP domain. These findings are consistent with the idea that amphiphysin's bulky IDP domain generates substantial steric pressure which, in collaboration with N-BAR scaffold assembly, drives membrane fission.

Our finding that modestly-curved F-BAR domains can also collaborate with bulky IDPs to drive potent fission is intriguing, as it suggests that proteins like FCHo1/2 may participate in membrane shaping throughout the lifetime of clathrin-coated pits, and may even help drive the final fission event. This hypothesis is in contrast to the idea that FCHo1/2 are primarily involved in the initiation of clathrin-coated pits[13, 48]. However, data from the Merrifield group showed that FCHo1/2 are present throughout the lifetime of clathrin-coated pits[55], supporting the possible role of FCHo1/2 in membrane shaping. Moreover, many F-BAR proteins involved in other cellular pathways such as cytokinesis also contain large regions of intrinsic disorder[15, 44, 45]. Our findings suggest that F-BAR scaffolds may facilitate membrane fission in a variety of contexts beyond membrane traffic.

More broadly, our work raises the possibility that protein assemblies beyond BAR domains may serve as scaffolds for crowding bulky IDPs in order to ensure efficient membrane fission. One potential example is dynamin, a GTPase involved in fission of clathrin-coated pits[56]. While dynamin itself does not contain substantial regions of disorder, it recruits proteins that contain large IDP domains, including amphiphysin and SNX9[57], which may generate significant steric pressure at membrane necks. In line with this thinking, in vitro studies from the Schmid and McMahon groups found that amphiphysin acts synergistically with dynamin to enhance membrane fission[54, 58]. Moreover, the yeast dynamin Vps1 is dispensable for fission in yeast cells, but is necessary for proper localization and accumulation of amphiphysin at clathrin-coated pits[52, 59]. An essential function of Vps1 may therefore be to organize and concentrate bulky IDP domains at membrane necks to ensure efficient fission, rather than driving fission directly. Another essential scaffold in membrane fission is ESCRT-III, which drives “reverse-topology” membrane fission in multivesicular body (MVB) biogenesis, cell division, and viral budding[60]. An important function of ESCRT-III in MVB formation may be to corral and concentrate cargo proteins, which often contain substantial bulk on the membrane leaflet opposite to the ESCRT-III polymers. Steric pressure among these cargo may help ensure potent membrane budding, a hypothesis that has been proposed in recent studies[61, 62].

Our work reveals a powerful synergistic relationship between structured protein assemblies and disordered pressure generators, which can be harnessed to drive membrane fission. It is increasingly recognized that structural disorder is prevalent in membrane trafficking, and that disordered domains are often coupled to structured domains within the same protein molecules[63]. While previous work has focused primarily on structure-function relationships revealed by studying isolated protein domains, future work should examine the collective contributions from both structure and disorder to understand how proteins shape membranes in diverse cellular contexts.

Acknowledgements
J.C.S. acknowledges funding from the National Institutes of Health (R01GM112065), including an administrative supplement for diversity in support of W. F. Z. W.T.S. acknowledges the support of a Ruth L. Kirschstein NRSA Predoctoral Fellowship from the National Institutes of Health (F31GM121013), as well as a fellowship from the Graduate School at UT Austin. G. K. acknowledges the support of a National Science Foundation Graduate Research Fellowship. We thank Dr. Anjon Audhya of the University of Wisconsin, Madison for advice on the purification of full-length FCHo1. We thank Liping Wang (Lafer lab, UT Health Science Center at San Antonio) for assistance with protein purification. We thank Dr. Darryl Sasaki (Sandia National Laboratories, Livermore, CA) for providing DP-EG10-biotin. We thank Dr. Gaudenz Danuser and Dr. Sandra Schmid (UT Southwestern, Dallas, TX) for freely providing cmeAnalysis particle detection software. We thank Dr. Dwight Romanovicz and the ICMB Microscopy Facility at UT Austin for assistance with electron microscopy.

Competing Financial Interests
The authors declare no competing financial interests.

Author Contributions
W.T.S., W.F.Z., G.K., R.W.P., and J.C.S. designed and performed membrane-protein interaction experiments. W.T.S., G.K., JB.R., and E.M.L. performed experiments to optimize expression and purification of recombinant proteins, including full-length proteins and unique protein chimeras. All authors consulted on the data and wrote the manuscript.

Supplementary Information

BAR scaffolds drive membrane fission by crowding disordered domains

Wilton T. Snead [a], Wade F. Zeno [a], Grace Kago [a], Ryan W. Perkins [a], J Blair Richter [b], Eileen M. Lafer [b], Jeanne C. Stachowiak [a,c,1]

Affiliations

[a] Department of Biomedical Engineering, The University of Texas at Austin, Austin, TX, 78712, USA; [b] Department of Biochemistry and Structural Biology, Center for Biomedical Neuroscience, The University of Texas Health Science Center at San Antonio, San Antonio, TX, 78212, USA; [c] Institute for Cellular and Molecular Biology, The University of Texas at Austin, Austin, TX, 78712, USA

[1] To whom correspondence should be addressed:
Jeanne C. Stachowiak (jcstach@austin.utexas.edu).

Supplementary Materials and Methods

Chemical reagents

MOPS (3-(N-morpholino)propanesulphonic acid), HEPES (4-(2-hydroxyethyl)-1-piperazineethanesulphonic acid), Tris hydrochloride, NaCl, DTT (dithiothreitol), IPTG (isopropyl-β-D-thiogalactopyranoside), β-mercaptoethanol, thrombin protease, and Triton X-100 were purchased from Fisher Scientific. EDTA (ethylenediaminetetraacetic acid), EGTA (ethylene glycol tetraacetic acid), TCEP (tris(2-carboxyethyl)phosphine hydrochloride), PMSF (phenylmethanesulfonyl fluoride), EDTA-free protease inhibitor tablets, Thrombin CleanCleave Kit, PLL (poly-L-lysine), Atto 488 NHS-ester, and Atto 594 NHS-ester were purchased from Sigma-Aldrich. HRV-3C (human rhinovirus-3C) protease, neutravidin, Oregon Green 488-DHPE (Oregon Green 488 1,2-dihexadecanoyl-*sn*-glycero-3-phosphoethanolamine), and Texas Red-DHPE were purchased from Thermo Fisher Scientific. mPEG-SVA (mPEG-succinimidyl valerate), biotin-PEG-SVA, mPEG-silane, and biotin-PEG-silane (all PEGs were molecular weight 5,000 Da) were purchased from Laysan Bio (Arab, AL, USA). DP-EG10-biotin (dipalmitoyl-decaethylene glycol-biotin) was generously provided by Dr. Darryl Sasaki of Sandia National Laboratories, Livermore, CA[64]. All other lipids were purchased from Avanti Polar Lipids (Alabaster, AL, USA), including: PtdIns(4,5)P_2 (L-α-phosphatidylinositol-4,5-bisphosphate, from porcine brain), DOGS-NTA-Ni (1,2-dioleoyl-sn-glycero-3-[(N-(5-amino-1-carboxypentyl)iminodiacetic acid)succinyl], nickel salt), DOPC (1,2-dioleoyl-sn-glycero-3-phosphocholine), and DOPS (1,2-dioleoyl-sn-glycero-3-phospho-L-serine, sodium salt). The lipid compositions for all experiments are listed in the figure captions.

Plasmids

The pGex6P bacterial expression vector containing full-length human amphiphysin (residues 2-695) was generously provided by the Baumgart Lab (University of Pennsylvania). The N-BAR domain of human amphiphysin (residues 2-242) was cloned into the pGex4T2 bacterial expression vector using BamHI and EcoRI restriction sites. The C-terminal domain of human amphiphysin lacking the SH3 domain (Amph CTD ΔSH3, residues 240-622) with N-terminal GST and 6his tags was cloned using a previously-generated plasmid template, GST-6his-AP180 CTD in pGex4T2[31]. AP180 CTD was excised from the template using SalI and XhoI restriction sites and the Amph CTD ΔSH3 insert was ligated in using the same SalI and XhoI sites. The N-BAR domain of human amphiphysin fused to the C-terminal domain of rat epsin1 (N-BAR-epsin CTD, residues 144-575 of rat epsin1) was cloned by first ligating in the N-BAR domain of human amphiphysin (residues 2-242) into pGex4T2 using BamHI and EcoRI restriction sites. Epsin CTD was then ligated in frame with N-BAR using SalI and NotI restriction sites. The I-BAR domain of human IRSp53 (residues 1-250) was cloned by using site directed mutagenesis to introduce a stop codon at residue 251 in the pGex6P2 plasmid containing full-length IRSp53. The I-BAR domain of human IRSp53 fused to the C-terminal domain of rat AP180 (I-BAR-AP180 CTD, residues 328-896 of rat AP180) was cloned by first ligating the I-BAR domain of human IRSp53 (residues 1-250) into pGex4T2 using BamHI and EcoRI restriction sites. AP180 CTD was then ligated in frame with I-BAR using SalI and XhoI restriction sites. The pGex6P1 vector containing full-length *C. elegans* FCHo1 (residues 1-968) was generously provided by the Audhya Lab (University of Wisconsin)[46]. The F-BAR domain of *C. elegans* FCHo1 (residues 1-276) was cloned into the pGex4T2 vector using BamHI and EcoRI restriction sites.

Protein purification

All proteins were expressed as N-terminal glutathione-S-transferase (GST) fusion constructs in BL21 *E. coli* cells following induction with 1 mM IPTG. Full-length amphiphysin, N-BAR, Amph CTD ΔSH3, I-BAR, I-BAR-AP180 CTD and F-BAR were induced for 6-8 h at 30 °C. N-BAR-epsin CTD was induced at 16 °C for 20 h. Full-length FCHo1 was induced at 12 °C for 24 h. Cells were harvested and bacteria were lysed using lysis buffer and probe sonication. For full-length FCHo1, lysis buffer was: 100 mM sodium phosphate pH 8.0, 5 mM EDTA, 5 mM DTT, 10% glycerol, 1 mM PMSF, 1% Triton X-100, 1x Roche protease inhibitor cocktail. For all other proteins, lysis buffer was: 500 mM Tris-HCl pH 8.0, 5 mM EDTA, 10 mM β-mercaptoethanol or 5 mM TCEP, 5% glycerol, 1 mM PMSF, 1% Triton X-100, 1x Roche or Pierce protease inhibitor cocktail. Proteins were purified from bacterial extracts by incubating with glutathione resin, followed by extensive washing (at least 10x column volumes). Full-length amphiphysin, N-BAR, Amph CTD ΔSH3, and F-BAR were cleaved directly from the resin using soluble HRV-3C

(Thermo Fisher) or thrombin (GE Healthcare Life Sciences) proteases overnight at 4 °C with rocking. HRV-3C, which contained a GST tag, was removed by passage through a glutathione agarose column. Thrombin was removed with *p*-aminobenzamidine-agarose resin (Sigma-Aldrich). N-BAR-epsin CTD, I-BAR, and I-BAR-AP180 CTD were eluted with 15 mM reduced glutathione in 500 mM Tris-HCl pH 8.0, 5 mM EDTA, 10 mM β-mercaptoethanol or 5 mM TCEP, 5% glycerol, 1 mM PMSF buffer. Full-length FCHo1 was eluted with 15 mM reduced glutathione in 100 mM sodium phosphate pH 8.0, 5 mM EDTA, 5 mM DTT, 10% glycerol, 1 mM PMSF buffer. The proteins were concentrated with EMD Millipore Amicon centrifugal filter units, desalted with Zeba Spin Desalting Columns (Fisher), and then incubated with either Thrombin CleanCleave Kit (Sigma-Aldrich), soluble HRV-3C, or soluble thrombin overnight at 4 °C with rocking. Cleaved GST was removed by passage through a glutathione agarose column. I-BAR-AP180 CTD and N-BAR-epsin CTD were further purified by gel filtration chromatography using a Superose 6 column equilibrated with 20 mM Tris-HCl pH 8.0, 150 mM NaCl, 1 mM EDTA, 5 mM EGTA, 1 mM PMSF, 5 mM DTT. All proteins were stored as small aliquots or liquid nitrogen pellets at -80 °C.

Protein labeling

Proteins were labeled using amine-reactive, NHS ester-functionalized dyes (Atto-Tec) in 25 mM HEPES pH 7.35, 150 mM NaCl, 5 mM TCEP buffer. The concentration of dye was adjusted experimentally to obtain the desired labeling ratio of 0.5-1 dye molecules per protein, typically 2-5 times molar excess of dye. Reactions were performed for 20-30 min at room temperature and labeled protein was separated from unconjugated dye using Princeton CentriSpin-20 size exclusion spin columns (Princeton Separations).

Transmission electron microscopy

Vesicles for electron microscopy were composed of 5 mol% PtdIns(4,5)P_2, 15 mol% DOPS, and 80 mol% DOPC. Dried lipid films were hydrated in 20 mM MOPS pH 7.35, 150 mM NaCl, 0.5 mM EGTA and EDTA buffer and extruded though a 200 nm pore filter (Whatman). Proteins were diluted to the indicated concentrations in the same MOPS buffer with 5 mM TCEP and incubated with vesicles at 37 °C for 30 min (Amph-FL and N-BAR) or 60 min (FCHo1-FL and F-BAR). The vesicle concentration was 1 mM in experiments with Amph-FL, FCHo1-FL, and F-BAR, and 0.1 mM in experiments with N-BAR and in protein-free controls. 5 µL of the mixture was placed onto a glow-discharged, 300 square mesh, carbon-coated grid and stained with 2% uranyl acetate (Electron Microscopy Sciences; Hatfield, PA, USA). Images were collected on a Tecnai Spirit BioTwin T12 electron microscope (Tecnai; Hillsboro, OR, USA). Vesicle and tubule diameters were measured using ImageJ software.

Fluorescence microscopy

A spinning disc confocal microscope (Zeiss Axio Observer Z1 with Yokagawa CSU-X1M) was used to image GUVs and tethered vesicles. Laser wavelengths of 488 and 561 nm were used for excitation. Emission filters were centered at 525 nm with a 50 nm width, and 629 nm with a 62 nm width. A triple-pass dichroic mirror was used: 405/488/561 nm. The microscope objective was a Plan-Apochromat 100x, 1.4 numerical aperture oil immersion objective. Images were collected on a cooled (-70 °C) EMCCD iXon3 897 camera (Andor Technology; Belfast, UK).

Giant unilamellar vesicle preparation

Giant unilamellar vesicles (GUVs) were prepared according to published protocols[65]. A mixture of 5 mol% PtdIns(4,5)P_2, 15 mol% DOPS, 0.5 mol% Oregon Green 488-DHPE, and 79.5 mol% DOPC was dried into a film on an indium-tin-oxide coated glass slide. Lipids were further dried under vacuum overnight. Electroformation was performed at 55 °C in 350 mOsm sucrose solution also containing 0.5 mM EGTA and EDTA to prevent clustering of PtdIns(4,5)P_2. Vesicles were mixed with protein solution at the specified concentration in 20 mM MOPS pH 7.35, 150 mM NaCl, 0.5 mM EGTA and EDTA, 5 mM TCEP buffer. Prior to mixing, the osmolarity of the GUV solution and experiment buffer was measured using a vapor pressure osmometer (Wescor).

SUPER template preparation

SUPER templates were prepared according to the protocol of Neumann et al[39]. A lipid mixture of 5 mol% PtdIns(4,5)P_2, 15 mol% DOPS, 1 mol% Texas Red DHPE, and 79 mol% DOPC was mixed in a clean glass test tube, the solvent was evaporated, and the lipid film was further dried under vacuum. The lipid film was hydrated in Milli-Q water, subjected to three freeze-thaw cycles in liquid nitrogen, and extruded through a 100 nm pore filter (Whatman). SUPER templates were made by creating a 100 µL mixture consisting of 200 µM liposomes, 1 M NaCl, and 5 x 10^6 of 2.5 µm m-type silica beads (Corpuscular; Cold Spring, NY, USA) in a low-adhesion microcentrifuge tube. The mixture was incubated for 30 min at room temperature and gently agitated periodically. The mixture was washed by adding 1 mL Milli-Q water, gently mixing, and spinning at 300 g for 2 min in a swinging bucket rotor to pellet the SUPER templates. 1 mL of supernatant was removed, SUPER templates were resuspended in the remaining 100 µL, and washing was repeated a total of four times. SUPER templates were kept on ice and used within 4 h.

Measurement of SUPER template membrane release

SUPER template membrane shedding experiments were performed according to the protocol of Neumann et al[39]. 10 µL of SUPER templates were gently pipetted into the top of a 90 µL solution of protein at specified concentrations in 20 mM MOPS pH 7.35, 150

mM NaCl, 0.5 mM EGTA and EDTA, 5 mM TCEP buffer. SUPER templates were allowed to slowly settle for 30 min at room temperature without disturbing. SUPER templates containing unreleased membrane were then sedimented by gentle centrifugation at 300 g for 2 min in a swinging bucket rotor. 75 µL of supernatant containing released membrane was collected and mixed in a 96-well plate with Triton X-100 at a final concentration of 0.1% and volume of 100 µL. In order to measure the total fluorescence of SUPER template membrane, a detergent control consisting of SUPER templates added directly to 0.1% Triton X-100, which solubilized all SUPER template membrane, was run. The fluorescence intensity of released membrane was measured in a plate reader using 590 nm excitation light and an emission filter centered at 620 nm. After subtracting the fluorescence of 0.1% Triton X-100 in buffer alone from all measurements, membrane release was calculated by dividing the fluorescence intensity after protein exposure by the fluorescence intensity of the detergent control. The background level of membrane release in the absence of protein was also measured by incubating SUPER templates in buffer alone. This buffer control was subtracted from all measurements as background.

Passivating glass coverslips with PEG and PEG-biotin for tethering vesicles

Glass coverslips were passivated by either directly conjugating PEG-silane and biotin-PEG-silane to the glass, or by coating the glass with a layer of poly-L-lysine (PLL) conjugated to PEG and biotin-PEG. For the direct silane conjugation, a 0.67% solution of PEG-silane was prepared in anhydrous isopropanol. Biotin-PEG-silane comprised 5% of the total amount of PEG-silane in the solution. The mixture was held in a bath sonicator for 10-15 min to dissolve the PEG. Acetic acid was added to a concentration of 1%, and 50 µL of the reactive mixture was dropped onto a dry, ultraclean coverslip. Another dry, ultraclean coverslip was sandwiched on top, and the slides were incubated at 70 °C for 30-60 min. The slides were separated, washed in ultrapure water, and stored dry for later use. Imaging wells were made by placing silicone gaskets onto the glass and hydrating in 20 mM MOPS pH 7.35, 150 mM NaCl buffer. Neutravidin was added to the well at a final concentration of 0.2 mg mL^{-1}, incubated for 10 min, and the well was washed repeatedly with MOPS buffer before adding vesicles.

The biotinylated PLL-PEG was made according to a previous protocol[66]. Briefly, amine-reactive PEG-SVA (succinimidyl valerate) and biotin-PEG-SVA was added to a 40 mg mL^{-1} mixture of PLL in 50 mM sodium tetraborate pH 8.5 at a molar ratio of one PEG per five lysine subunits. PEG-biotin comprised 2% of the total PEG amount. The mixture was stirred continuously for 6 h at room temperature and buffer exchanged into PBS using Centri-Spin size exclusion columns (Princeton Separations). Imaging wells were made by placing silicone gaskets onto ultraclean coverslips. Wells were coated for 20-30 min with biotinylated PLL-PEG diluted tenfold in 20 mM MOPS pH 7.35, 150 mM NaCl buffer. After

coating, the well was washed repeatedly with MOPS buffer to wash out excess PLL-PEG. Neutravidin was added to the well following the same process as for PEG-silane slides.

Determination of vesicle diameter from measurements of tethered vesicle brightness

Vesicle diameter distributions were measured using an assay developed by the Stamou group[67-69]. Vesicles in experiments with Amph-FL, N-BAR, N-BAR-epsin CTD, I-BAR-AP180 CTD, FCHo1-FL, and F-BAR were composed of 76 mol% DOPC, 15 mol% DOPS, 5 mol% PtdIns(4,5)P_2, 2 mol% DP-EG10-biotin, and 2 mol% Oregon Green 488-DHPE. Vesicles in experiments with Amph CTD ΔSH3 were composed of a similar lipid mixture, with the exception that DOPS and PtdIns(4,5)P_2 were replaced with 20 mol% DOGS-NTA-Ni. Dried lipid films were hydrated in 20 mM MOPS pH 7.35, 150 mM NaCl buffer (0.5 mM EGTA and EDTA was included in experiments with PtdIns(4,5)P_2) and extruded to 200 nm.

Fission experiments were performed by mixing vesicles at a concentration of 10 μM with unlabeled protein at specified concentrations in the above MOPS buffer with 5 mM TCEP. The mixture was incubated at 37 °C for either 30 min (Amph-FL, N-BAR, Amph CTD ΔSH3, and N-BAR-epsin CTD) or 60 min (I-BAR-AP180 CTD, FCHo1-FL, and F-BAR). During the incubation period, imaging wells were prepared as described above. After incubation, the mixtures were added to the wells and vesicles were allowed to tether for 10 min before washing repeatedly to remove untethered vesicles. Multiple spinning disc confocal z-stacks of tethered vesicles were acquired with a z-step of 0.1 μm. The same laser power and camera gain settings were used for all experiments.

All images in the z-stacks were cropped to the center 171x171 pixels (center 1/9th), and the frame with the greatest mean brightness was selected as the best focus image for analysis. Fluorescence amplitudes of diffraction-limited puncta were obtained using cmeAnalysis particle detection software[70]. Individual vesicles were detected by fitting two-dimensional Gaussian profiles to each puncta. The standard deviation of the Gaussian was determined from the point spread function of our microscope. The brightness values of detected puncta were reported as valid if they were diffraction-limited and had amplitudes significantly above their local fluorescence background. To further ensure that puncta were well above the noise threshold, we only accepted puncta that persisted at the same location through three consecutive imaging frames.

To convert fluorescence brightness values to vesicle diameters, we computed a scaling factor that centered the median of the vesicle brightness distribution, before protein exposure, to the intensity-weighted average vesicle diameter obtained from dynamic light

scattering. This same scaling factor was then used to scale the vesicle brightness distributions after protein exposure to distributions of vesicle diameter.

The vesicle diameter distributions shown in Fig. 2d-f, 3b,f, and 4i,j represent data pooled from three independent experiments. The markers in Fig. 2g, 3c,g, and 4k, which plot the proportion of vesicle diameters below 30 nm, show the mean ± first s.d. of the three independent experiments.

Determination of membrane coverage by proteins from measurements of vesicle and protein brightness

Vesicles in experiments with full-length amphiphysin and N-BAR were composed of 76 mol% DOPC, 15 mol% DOPS, 5 mol% PtdIns(4,5)P_2, 2 mol% DP-EG10-biotin, and 2 mol% Oregon Green 488-DHPE. DOPS and PtdIns(4,5)P_2 were replaced with 20 mol% DOGS-NTA-Ni in experiments with Amph CTD ΔSH3. Dried lipid films were hydrated in 20 mM MOPS pH 7.35, 150 mM NaCl buffer (0.5 mM EGTA and EDTA was included in experiments with PtdIns(4,5)P_2) and extruded to 30 or 200 nm. Imaging wells were prepared as described above. Vesicles were diluted to 5 μM in the wells and allowed to tether for 10 min. Untethered vesicles were removed by thorough washing with MOPS buffer. After tethering, Atto 594-labeled protein was added to the specified concentration, and multiple spinning disc confocal z-stacks of lipid and protein fluorescence were acquired, with a z-step of 0.1 μm. Images were collected after approximately 15 min incubation of protein with vesicles. The same laser power and camera gain settings were used for all experiments. Supplementary Fig. S2a shows images of tethered vesicles with 10 and 25 nM Amph-FL-Atto 594, demonstrating increased protein brightness (and therefore membrane coverage) with increasing protein concentration.

Images were cropped and individual vesicle puncta were detected using cmeAnalysis software[70], following the same approach described in the previous section. Here the algorithm also searched for fluorescent puncta in the protein channel using the centroids of the detected fluorescent puncta in the master lipid channel. The search region in the protein channel was three times the standard deviation of the Gaussian fit to the point spread function of our microscope. We estimated vesicle diameters from lipid fluorescence brightnesses by calibrating against dynamic light scattering, as described in the previous section. We estimated the number of bound proteins on each vesicle by comparing brightness values in the protein channel to the brightness of a single molecule of Atto 594-labeled protein. Images of single molecules of Atto 594-labeled proteins were obtained by adding a dilute concentration of protein to an imaging well on an ultraclean coverslip, and imaging single proteins adhered to the coverslip surface in a similar manner as described for the tethered vesicles. A linear correction for camera exposure time was applied to the single molecule brightness, as longer exposure times were

required to image single molecules compared to membrane-bound protein. Supplementary Fig. S2b shows a plot of the raw protein intensity values as a function of vesicle intensity for 10 and 25 nM Amph-FL. The 25 nM data shows a higher slope than 10 nM, indicating greater membrane coverage. Supplementary Fig. S2c shows this same data after processing, plotted as the number of membrane-bound proteins as a function of vesicle diameter.

Membrane coverage by proteins was estimated for each vesicle by dividing the area occupied by membrane-bound proteins by the corresponding vesicle surface area. The projected membrane footprint of N-BAR, Amph-FL, and Amph CTD ΔSH3 monomers were assumed to be: 25, 95, and 95 nm^2, respectively. The average membrane coverage within an experiment was estimated as the mean of all individual vesicle coverage values. Experiments were repeated three times for each protein concentration. Supplementary Fig. S2d,e and Fig. 3d plots the mean ± first s.d. of the coverage values from the three experiments. To confirm the validity of this analysis approach, we also plotted the area of membrane-bound proteins as a function of vesicle surface area, as shown in Supplementary Fig. S4c for the 1 μM Amph CTD ΔSH3 dataset. The slope of a linear fit to these data provides an alternative estimate of membrane coverage. The slope of 0.26, or 26% coverage, agrees well with the 29% membrane coverage value in Fig. 3d that was estimated using the method described above.

Supplementary Fig. S2d,e plots membrane coverage of N-BAR and Amph-FL at 5, 10, and 25 nM, indicating similar binding behavior of each protein within this concentration regime. At concentrations above 25 nM, Amph-FL significantly deformed and tubulated 200 nm tethered vesicles, leading to inaccuracies in coverage estimates. Therefore, to obtain estimates of membrane coverage by Amph-FL at higher concentrations at which potent fission occurs, we used higher initial curvature vesicles, extruded to 30 nm. Supplementary Fig. S2f plots membrane coverage by Amph-FL at 25 and 100 nM on 30 nm vesicles, showing that Amph-FL reaches approximately 93% membrane coverage at 100 nM, significantly higher than can be reached by protein monomers that do not assemble[42]. This coverage is expected to generate significant steric pressure from IDP crowding, thus providing a potential explanation for the strong membrane fission observed with Amph-FL at 100 nM.

Supplementary Figures

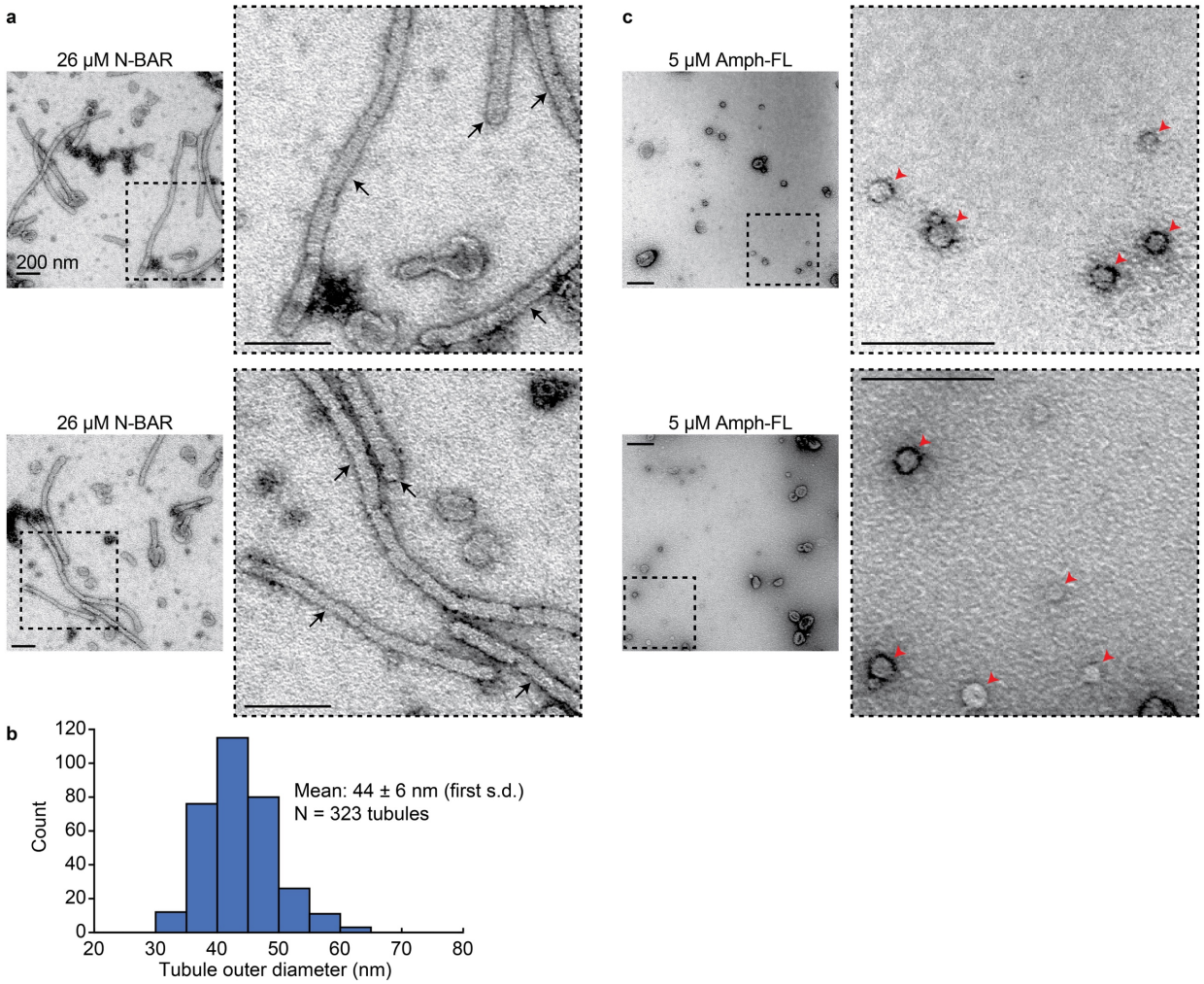

Figure S1. Transmission electron microscopy reveals that while N-BAR generates membrane tubules, Amph-FL forms highly curved fission vesicles. Vesicle composition: 80 mol% DOPC, 5 mol% PtdIns(4,5)P_2, 15 mol% DOPS, extruded to 200 nm. (**a**) Two representative electron micrographs of tubules generated by 26 μM N-BAR. Dashed boxes indicate zoomed regions to the right of each image. (**b**) Histogram of tubule outer diameters generated by 26 μM N-BAR. Mean = 44 ± 6 nm first s.d., n = 323 tubules. (**c**) Two representative electron micrographs of fission vesicles generated by 5 μM Amph-FL. Dashed boxes indicate zoomed regions to the right of each image. Black arrows indicate tubules, red arrowheads indicate fission vesicles. All scale bars, including zoomed regions: 200 nm.

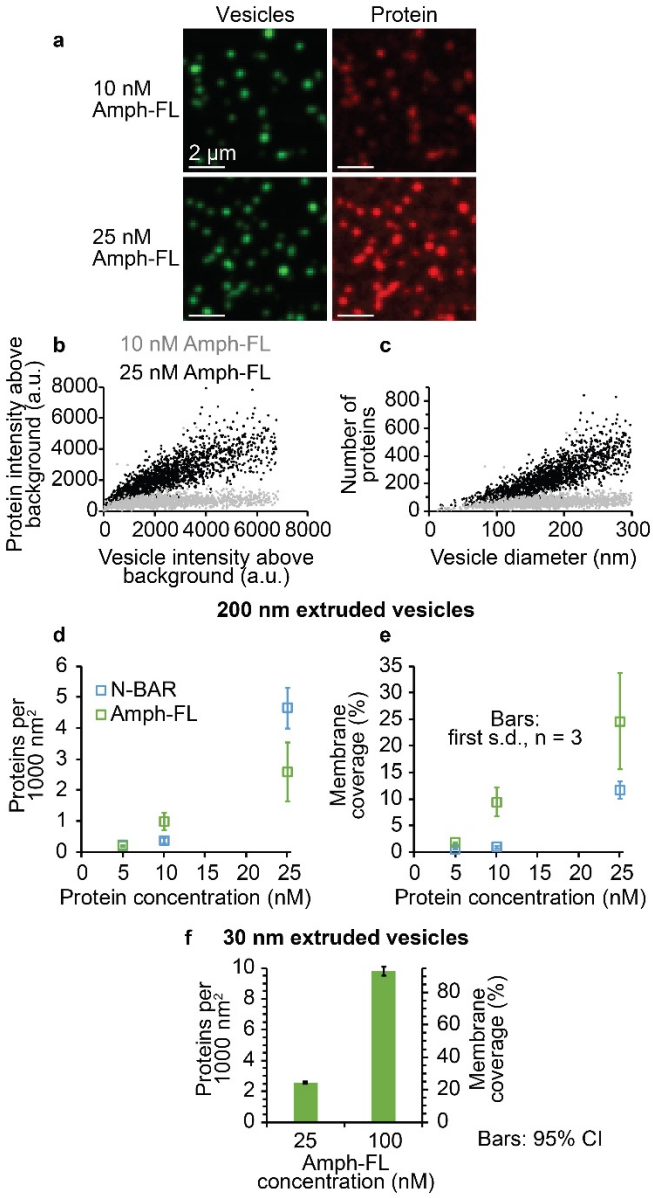

Figure S2. Membrane coverage measurements reveal that N-BAR and Amph-FL bind to membranes with similar affinity, and that Amph-FL reaches a highy crowded coverage when fission occurs. Vesicle composition: 76 mol% DOPC, 15 mol% DOPS, 5 mol% PtdIns(4,5)P_2, 2 mol% DP-EG10-biotin, and 2 mol% Oregon Green 488-DHPE. (a-e): Extruded to 200 nm. (f): Extruded to 30 nm. (**a**) Images of tethered vesicles (green, left column) and membrane-bound Amph-FL-Atto 594 (red, right column). Top row is 10 nM, bottom row is 25 nM. Images in each column have equal contrast to show that increasing protein concentration leads to increased membrane-bound protein intensity. (**b**) Plot of raw protein intensity values as a function of vesicle intensity for 10 and 25 nM Amph-FL. The 25 nM data show a greater slope, indicating increased coverage by proteins. (**c**) The same data in (b) after processing (see methods), now plotted as the number of membrane-bound proteins as a function of vesicle diameter. (**d**) Plot of the number of membrane-bound proteins per 1000 nm^2 of membrane surface area as a function of the concentration of N-BAR or Amph-FL. The two proteins follow

a similar trend, indicating similar binding. (**e**) Data in (d) plotted as the coverage of the membrane surface by proteins as a function of protein concentration. Because Amph-FL occupies a greater area on the membrane surface compared to N-BAR (95 versus 25 nm^2 per monomer, respectively), Amph-FL reaches a higher coverage than N-BAR at equal number density of membrane-bound proteins. At 25 nM, Amph-FL reaches approximately 25% membrane coverage, approaching a crowded regime[24, 32]. Markers in (d) and (e) represent mean ± first s.d., n = 3 independent experiments. (**f**) Membrane coverage estimates for 25 and 100 nM Amph-FL on 30 nm vesicles. At 100 nM Amph-FL, when potent membrane fission occurs, Amph-FL reaches approximately 93% membrane coverage, significantly higher than can be reached by non-assembling proteins. At this coverage, steric pressure from disordered domain crowding is very high, providing a potential explanation for strong membrane fission by Amph-FL. Markers indicate mean of all coverage values, error bars represent 95% confidence interval. 25 nM: n = 2,171 vesicles, 100 nM: n = 1,783 vesicles. Scale bars in (a): 2 µm.

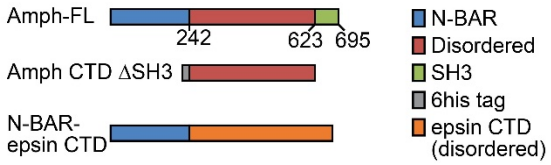

Figure S3. Domain diagrams of Amph-FL, Amph CTD ΔSH3, and N-BAR-epsin CTD.

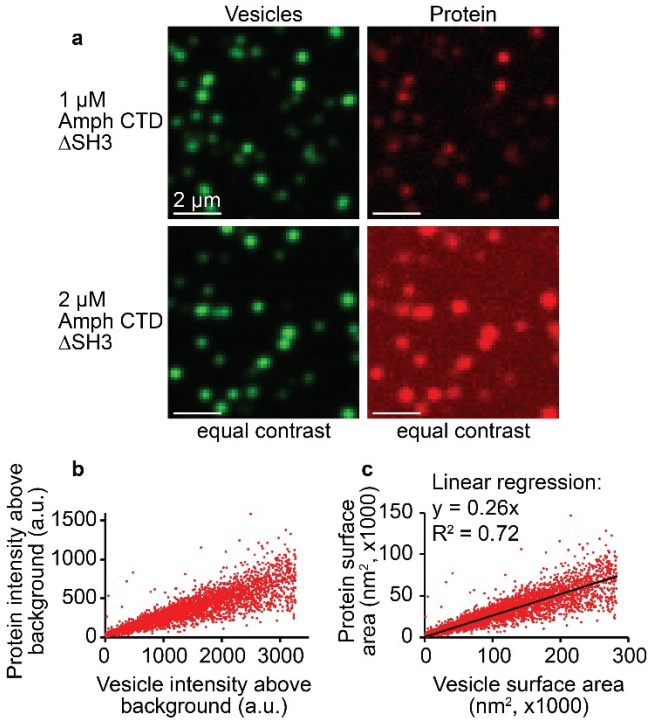

Figure S4. Membrane coverage experiments reveal that Amph CTD ΔSH3 requires higher protein concentration to reach comparable coverage to Amph-FL. Vesicle composition: 76 mol% DOPC, 20 mol% DOGS-NTA-Ni, 2 mol% DP-EG10-biotin, and 2 mol% Oregon Green 488-DHPE, extruded to 200 nm. (**a**) Images of tethered vesicles (green, left column) and membrane-bound Amph CTD ΔSH3-Atto 594 (red, right column). Top row is 1 μM, bottom row is 2 μM. Images in each column have equal contrast to show greater protein intensity with increasing concentration. (**b**) Plot of raw protein intensity values as a function of vesicle intensity for the 1 μM Amph CTD ΔSH3 dataset. (**c**) Plot of the same 1 μM Amph CTD ΔSH3 dataset after processing, plotted here as the area occupied by membrane-bound proteins as a function of vesicle surface area. The slope of a linear fit to the data represents the average membrane coverage by proteins. The value of 26% coverage from this approach agrees with 29% membrane coverage shown in Fig. 3d, estimated by averaging all of the membrane coverage values of individual vesicles. Scale bars in (a): 2 μm.

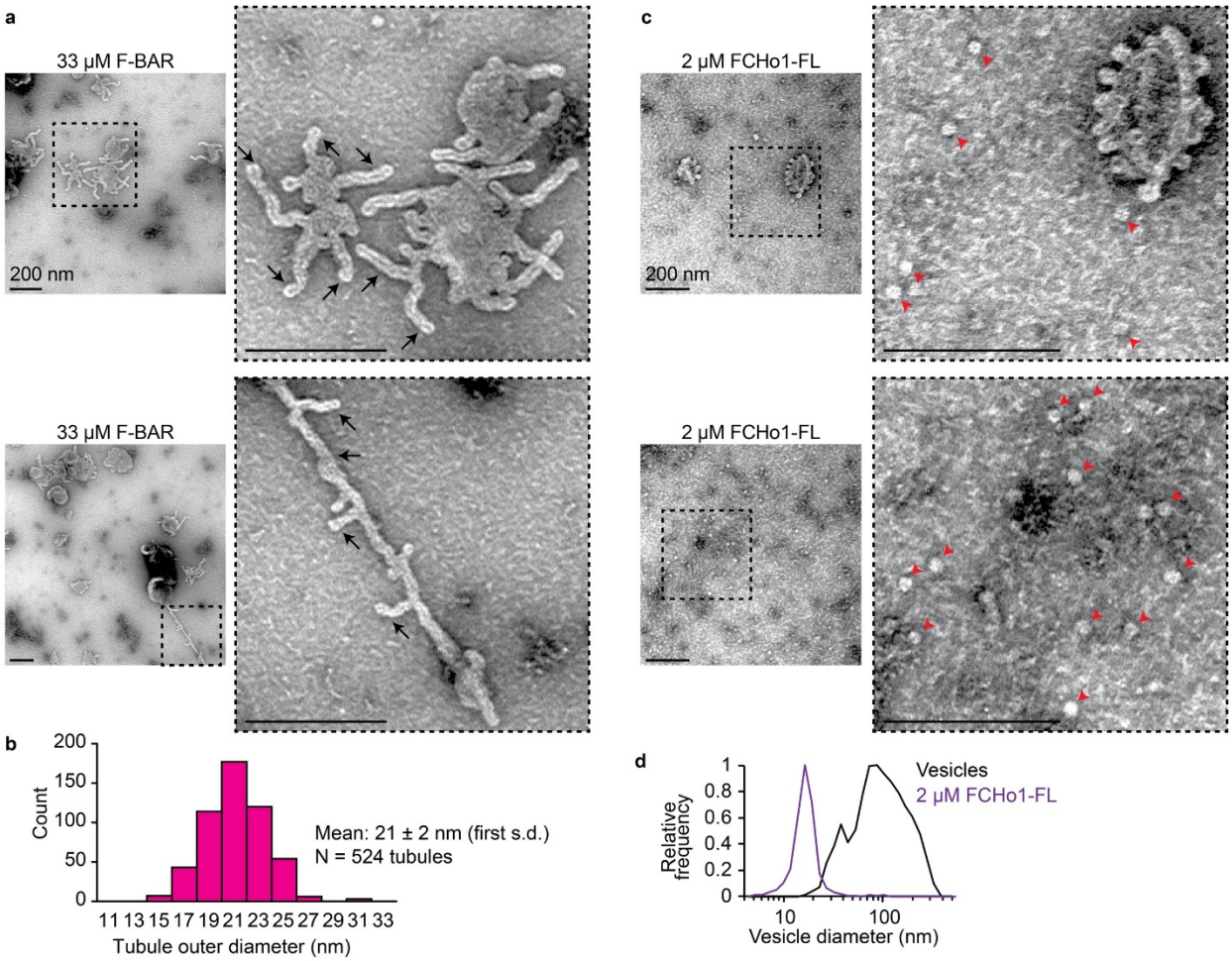

Figure S5. Transmission electron microscopy reveals that while F-BAR generates membrane tubules, FCHo1-FL forms highly curved fission products. Vesicle composition: 80 mol% DOPC, 5 mol% PtdIns(4,5)P_2, 15 mol% DOPS, extruded to 200 nm. (**a**) Two representative electron micrographs of tubules generated by 33 μM F-BAR. Dashed boxes indicate zoomed

regions to the right of each image. (**b**) Histogram of the outer diameters of tubules generated by 33 μM F-BAR. Mean = 21 ± 2 nm first s.d., n = 524 tubules. (**c**) Two representative electron micrographs of fission vesicles generated by 2 μM FCHo1-FL. Dashed boxes indicate zoomed regions to the right of each image. The top zoomed region shows a larger vesicle with highly curved buds extending from the surface, which may be an intermediate state prior to full fission. (**d**) Histograms of vesicle diameters before and after exposure to 2 μM FCHo1-FL. FCHo1-FL generates a high-curvature vesicle population with average diameter 17 ± 7 nm first s.d. Vesicles alone: n = 1,302 vesicles. 2 μM FCHo1-FL: n = 1,676 vesicles. Black arrows indicate tubules, red arrowheads indicate fission vesicles. All scale bars, including zoomed regions: 200 nm.

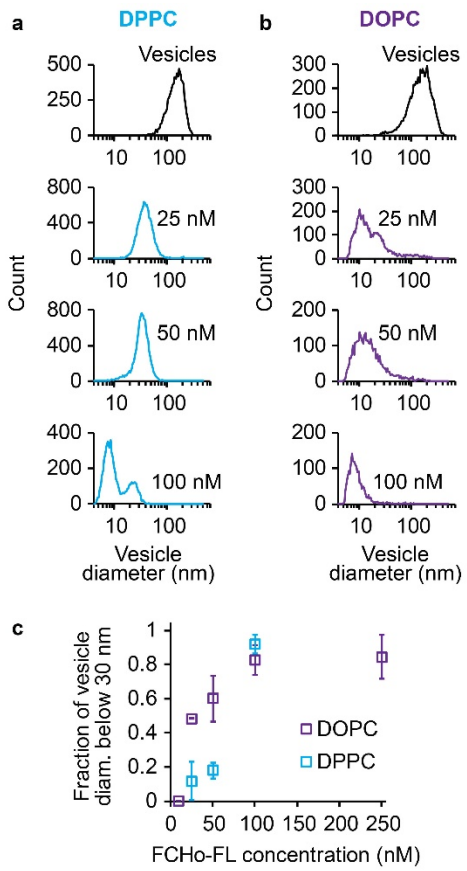

Figure S6. Increasing bilayer rigidity results in lower-curvature fission products generated by FCHo1-FL. Vesicle composition in (a): 76 mol% DPPC, 15 mol% DPPS, 5 mol% PtdIns(4,5)P_2, 2 mol% DP-EG10-biotin, and 2 mol% Oregon Green 488-DHPE. For vesicles in (b), DPPC and DPPS were replaced with DOPC and DOPS, respectively. All vesicles extruded to 200 nm. (**a**) Fission product diameter distributions from tethered vesicle fission assay with DPPC as the primary lipid after exposure to 25, 50, and 100 nM FCHo1-FL. (**b**) Fission product diameter distributions with DOPC as the primary lipid after 25, 50, and 100 nM FCHo1-FL, repeated from Fig. 4i. DPPC fission product distributions in (a) show lower-curvature fission products compared to the high-curvature populations with DOPC vesicles in

(b), indicating that increasing the bilayer rigidity restricts micelle formation by FCHo1-FL. (**c**) Plot of the proportion of fission product diameters below 30 nm as a function of FCHo1-FL concentration. DPPC vesicles require higher FCHo1-FL concentration to observe high-curvature fission products observed with DOPC vesicles. DOPC data repeated from Fig. 4k.

Supplementary Video Legends

Supplementary Video 1. The amphiphysin N-BAR domain generates mobile lipid tubules from GUVs. GUV composition: 79.5 mol% DOPC, 5 mol% PtdIns(4,5)P_2, 15 mol% DOPS, 0.5 mol% Oregon Green 488-DHPE. GUVs were mixed with 5 μM N-BAR and imaged by confocal microscopy. Fluorescence signal comes from Atto594-labeled protein. The frames are approximately 400 ms apart. The video plays at 5 frames per second.

Supplementary Video 2. Full-length amphiphysin generates mobile lipid tubules from GUVs. GUV composition: 79.5 mol% DOPC, 5 mol% PtdIns(4,5)P_2, 15 mol% DOPS, 0.5 mol% Oregon Green 488-DHPE. GUVs were mixed with 5 μM Amph-FL and imaged by confocal microscopy. Fluorescence signal comes from Atto594-labeled protein. The frames are approximately 400 ms apart. The video plays at 5 frames per second.

Supplementary Video 3. The amphiphysin N-BAR domain drives collapsing of vesicles into diffraction-limited tubules and fragments. GUV composition: 79.5 mol% DOPC, 5 mol% PtdIns(4,5)P_2, 15 mol% DOPS, 0.5 mol% Oregon Green 488-DHPE. GUVs were mixed with 5 μM N-BAR and imaged by confocal microscopy. Fluorescence signal comes from Atto594-labeled protein. The frames are approximately 400 ms apart. The video plays at 5 frames per second.

Supplementary Video 4. Full-length amphiphysin drives collapsing of vesicles into diffraction-limited tubules and fragments. GUV composition: 79.5 mol% DOPC, 5 mol% PtdIns(4,5)P_2, 15 mol% DOPS, 0.5 mol% Oregon Green 488-DHPE. GUVs were mixed with 5 μM Amph-FL and imaged by confocal microscopy. Fluorescence signal comes from Atto594-labeled protein. The frames are approximately 400 ms apart. The video plays at 5 frames per second.

Supplementary Video 5. The IRSp53 I-BAR domain drives inward tubulation. GUV composition: 79.5 mol% DOPC, 5 mol% PtdIns(4,5)P_2, 15 mol% DOPS, 0.5 mol% Oregon Green 488-DHPE. GUVs were mixed with 5 μM I-BAR and imaged by confocal microscopy. Fluorescence signal comes from Atto594-labeled protein. The frames are approximately 500 ms apart. The video plays at 5 frames per second.

Supplementary Video 6. The I-BAR-AP180 CTD chimera drives frustrated membrane fluctuations. GUV composition: 79.5 mol% DOPC, 5 mol% PtdIns(4,5)P_2, 15 mol% DOPS, 0.5 mol% Oregon Green 488-DHPE. GUVs were mixed with 10 μM I-BAR-AP180 CTD and imaged by confocal microscopy. Fluorescence signal comes from Atto594-labeled protein. The frames are approximately 500 ms apart. The video plays at 5 frames per second.

References

1. Conner, S. & Schmid, S. Regulated portals of entry into the cell. *Nature* **422**, 37-44 (2003).

2. Hurley, J., Boura, E., Carlson, L. & Rozycki, B. Membrane Budding. *Cell* **143**, 875-887 (2010).

3. Mierzwa, B. & Gerlich, D. Cytokinetic Abscission: Molecular Mechanisms and Temporal Control. *Developmental Cell* **31**, 525-538 (2014).

4. Helfrich, W. Elastic Properties of Lipid Bilayers - Theory and Possible Experiments. *Zeitschrift Fur Naturforschung C-a Journal of Biosciences* **C 28**, 693-703 (1973).

5. Zimmerberg, J. & Kozlov, M. How proteins produce cellular membrane curvature. *Nature Reviews Molecular Cell Biology* **7**, 9-19 (2006).

6. Frost, A., Unger, V. & De Camilli, P. The BAR Domain Superfamily: Membrane-Molding Macromolecules. *Cell* **137**, 191-196 (2009).

7. Mim, C. & Unger, V. Membrane curvature and its generation by BAR proteins. *Trends in Biochemical Sciences* **37**, 526-533 (2012).

8. Simunovic, M., Voth, G., Callan-Jones, A. & Bassereau, P. When Physics Takes Over: BAR Proteins and Membrane Curvature. *Trends in Cell Biology* **25**, 780-792 (2015).

9. McMahon, H. & Gallop, J. Membrane curvature and mechanisms of dynamic cell membrane remodelling. *Nature* **438**, 590-596 (2005).

10. Boucrot, E. *et al.* Membrane Fission Is Promoted by Insertion of Amphipathic Helices and Is Restricted by Crescent BAR Domains. *Cell* **149**, 124-136 (2012).

11. Peter, B. *et al.* BAR domains as sensors of membrane curvature: The amphiphysin BAR structure. *Science* **303**, 495-499 (2004).

12. Henne, W. *et al.* Structure and analysis of FCHo2 F-BAR domain: A dimerizing and membrane recruitment module that effects membrane curvature. *Structure* **15**, 839-852 (2007).

13. Henne, W. *et al.* FCHo Proteins Are Nucleators of Clathrin-Mediated Endocytosis. *Science* **328**, 1281-1284 (2010).

14. Guerrier, S. *et al.* The F-BAR Domain of srGAP2 Induces Membrane Protrusions Required for Neuronal Migration and Morphogenesis. *Cell* **138**, 990-1004 (2009).

15. McDonald, N. *et al.* The Tubulation Activity of a Fission Yeast F-BAR Protein Is Dispensable for Its Function in Cytokinesis. *Cell Reports* **14**, 534-546 (2016).

16. McDonald, N., Kooi, C., Ohi, M. & Gould, K. Oligomerization but Not Membrane Bending Underlies the Function of Certain F-BAR Proteins in Cell Motility and Cytokinesis. *Developmental Cell* **35**, 725-736 (2015).

17. Mattila, P. *et al.* Missing-in-metastasis and IRSp53 deform PI(4,5)P-2-rich membranes by an inverse BAR domain-like mechanism. *Journal of Cell Biology* **176**, 953-964 (2007).

18. Saarikangas, J. *et al.* Molecular Mechanisms of Membrane Deformation by I-BAR Domain Proteins. *Current Biology* **19**, 95-107 (2009).

19. Miele, A., Watson, P., Evans, P., Traub, L. & Owen, D. Two distinct interaction motifs in amphiphysin bind two independent sites on the clathrin terminal domain beta-propeller. *Nature Structural & Molecular Biology* **11**, 242-248 (2004).

20. Wuertenberger, S. & Groemping, Y. A single PXXP motif in the C-terminal region of srGAP3 mediates binding to multiple SH3 domains. *Febs Letters* **589**, 1156-1163 (2015).

21. Roberts-Galbraith, R. & Gould, K. Setting the F-BAR Functions and regulation of the F-BAR protein family. *Cell Cycle* **9**, 4091-4097 (2010).

22. Lee, S. *et al.* Structural basis for the actin-binding function of missing-in-metastasis. *Structure* **15**, 145-155 (2007).

23. Stachowiak, J., Hayden, C. & Sasaki, D. Steric confinement of proteins on lipid membranes can drive curvature and tubulation. *Proceedings of the National Academy of Sciences of the United States of America* **107**, 7781-7786 (2010).

24. Stachowiak, J. *et al.* Membrane bending by protein-protein crowding. *Nature Cell Biology* **14**, 944-949 (2012).

25. Copic, A., Latham, C., Horlbeck, M., D'Arcangelo, J. & Miller, E. ER Cargo Properties Specify a Requirement for COPII Coat Rigidity Mediated by Sec13p. *Science* **335**, 1359-1362 (2012).

26. Jiang, Z., de Messieres, M. & Lee, J. Membrane Remodeling by alpha-Synuclein and Effects on Amyloid Formation. *Journal of the American Chemical Society* **135**, 15970-15973 (2013).

27. Vennema, H. *et al.* Nucleocapsid-independent assembly of coronavirus-like particles by co-expression of viral envelope protein genes. *Embo Journal* **15**, 2020-2028 (1996).

28. Wu, T., Shi, Z. & Baumgart, T. Mutations in BIN1 Associated with Centronuclear Myopathy Disrupt Membrane Remodeling by Affecting Protein Density and Oligomerization. *Plos One* **9** (2014).

29. Bhagatji, P., Leventis, R., Comeau, J., Refaei, M. & Silvius, J. Steric and not structure-specific factors dictate the endocytic mechanism of glycosylphosphatidylinositol-anchored proteins. *Journal of Cell Biology* **186**, 615-628 (2009).

30. Hofmann, H. *et al.* Polymer scaling laws of unfolded and intrinsically disordered proteins quantified with single-molecule spectroscopy. *Proceedings of the National Academy of Sciences of the United States of America* **109**, 16155-16160 (2012).

31. Busch, D. *et al.* Intrinsically disordered proteins drive membrane curvature. *Nature Communications* **6** (2015).

32. Snead, W. *et al.* Membrane fission by protein crowding. *Proceedings of the National Academy of Sciences of the United States of America* **114**, E3258-E3267 (2017).

33. Owen, D., Collins, B. & Evans, P. Adaptors for clathrin coats: Structure and function. *Annual Review of Cell and Developmental Biology* **20**, 153-191 (2004).

34. Owen, D. *et al.* Crystal structure of the amphiphysin-2 SH3 domain and its role in the prevention of dynamin ring formation. *Embo Journal* **17**, 5273-5285 (1998).

35. Gallop, J. *et al.* Mechanism of endophilin N-BAR domain-mediated membrane curvature. *Embo Journal* **25**, 2898-2910 (2006).

36. Campelo, F., Malhotra, V. & Kornberg, R. Membrane Fission: The Biogenesis of Transport Carriers. *Annual Review of Biochemistry, Vol 81* **81**, 407-427 (2012).

37. Pucadyil, T. & Schmid, S. Real-Time Visualization of Dynamin-Catalyzed Membrane Fission and Vesicle Release. *Cell* **135**, 1263-1275 (2008).

38. Liu, Y. *et al.* Differential curvature sensing and generating activities of dynamin isoforms provide opportunities for tissue-specific regulation. *Proceedings of the National Academy of Sciences of the United States of America* **108**, E234-E242 (2011).

39. Neumann, S., Pucadyil, T. & Schmid, S. Analyzing membrane remodeling and fission using supported bilayers with excess membrane reservoir. *Nature Protocols* **8**, 213-222 (2013).

40. Sorre, B. *et al.* Nature of curvature coupling of amphiphysin with membranes depends on its bound density. *Proceedings of the National Academy of Sciences of the United States of America* **109**, 173-178 (2012).

41. Simunovic, M. *et al.* How curvature-generating proteins build scaffolds on membrane nanotubes. *Proceedings of the National Academy of Sciences of the United States of America* **113**, 11226-11231 (2016).

42. Feder, J. Random sequential adsorption. *Journal of Theoretical Biology* **87**, 237-254 (1980).

43. Reider, A. *et al.* Syp1 is a conserved endocytic adaptor that contains domains involved in cargo selection and membrane tubulation. *Embo Journal* **28**, 3103-3116 (2009).

44. Roberts-Galbraith, R. *et al.* Dephosphorylation of F-BAR Protein Cdc15 Modulates Its Conformation and Stimulates Its Scaffolding Activity at the Cell Division Site. *Molecular Cell* **39**, 86-99 (2010).

45. Meitinger, F. *et al.* Phosphorylation-dependent regulation of the F-BAR protein Hof1 during cytokinesis. *Genes & Development* **25**, 875-888 (2011).

46. Wang, L., Johnson, A., Hanna, M. & Audhya, A. Eps15 membrane-binding and -bending activity acts redundantly with Fcho1 during clathrin-mediated endocytosis. *Molecular Biology of the Cell* **27**, 2675-2687 (2016).

47. Umasankar, P. *et al.* A clathrin coat assembly role for the muniscin protein central linker revealed by TALEN-mediated gene editing. *Elife* **3** (2014).

48. Ma, L. *et al.* Transient Fcho1/2.Eps15/R.AP-2 Nanoclusters Prime the AP-2 Clathrin Adaptor for Cargo Binding. *Developmental Cell* **37**, 428-443 (2016).

49. Frolov, V., Escalada, A., Akimov, S. & Shnyrova, A. Geometry of membrane fission. *Chemistry and Physics of Lipids* **185**, 129-140 (2015).

50. Dimova, R. Recent developments in the field of bending rigidity measurements on membranes. *Advances in Colloid and Interface Science* **208**, 225-234 (2014).

51. Lee, C., Lin, W. & Wang, J. All-optical measurements of the bending rigidity of lipid-vesicle membranes across structural phase transitions. *Physical Review E* **64** (2001).

52. Kaksonen, M., Toret, C. & Drubin, D. A modular design for the clathrin- and actin-mediated endocytosis machinery. *Cell* **123**, 305-320 (2005).

53. Kishimoto, T. *et al.* Determinants of endocytic membrane geometry, stability, and scission. *Proceedings of the National Academy of Sciences of the United States of America* **108**, E979-E988 (2011).

54. Meinecke, M. *et al.* Cooperative Recruitment of Dynamin and BIN/Amphiphysin/Rvs (BAR) Domain-containing Proteins Leads to GTP-dependent Membrane Scission. *Journal of Biological Chemistry* **288**, 6651-6661 (2013).

55. Taylor, M., Perrais, D. & Merrifield, C. A High Precision Survey of the Molecular Dynamics of Mammalian Clathrin-Mediated Endocytosis. *Plos Biology* **9** (2011).

56. Antonny, B. *et al.* Membrane fission by dynamin: what we know and what we need to know. *Embo Journal* **35**, 2270-2284 (2016).

57. Daumke, O., Roux, A. & Haucke, V. BAR Domain Scaffolds in Dynamin-Mediated Membrane Fission. *Cell* **156**, 882-892 (2014).

58. Neumann, S. & Schmid, S. Dual Role of BAR Domain-containing Proteins in Regulating Vesicle Release Catalyzed by the GTPase, Dynamin-2. *Journal of Biological Chemistry* **288**, 25119-25128 (2013).

59. Smaczynska-de Rooij, I. *et al.* A role for the dynamin-like protein Vps1 during endocytosis in yeast. *Journal of Cell Science* **123**, 3496-3506 (2010).

60. Schoneberg, J., Lee, I., Iwasa, J. & Hurley, J. Reverse-topology membrane scission by the ESCRT proteins. *Nature Reviews Molecular Cell Biology* **18**, 5-17 (2017).

61. Chiaruttini, N. *et al.* Relaxation of Loaded ESCRT-III Spiral Springs Drives Membrane Deformation. *Cell* **163**, 866-879 (2015).

62. Adell, M. *et al.* Recruitment dynamics of ESCRT-III and Vps4 to endosomes and implications for reverse membrane budding. *Elife* **6** (2017).

63. Pietrosemoli, N., Pancsa, R. & Tompa, P. Structural Disorder Provides Increased Adaptability for Vesicle Trafficking Pathways. *Plos Computational Biology* **9** (2013).

64. Momin, N. *et al.* Designing lipids for selective partitioning into liquid ordered membrane domains. *Soft Matter* **11**, 3241-3250 (2015).

65. Angelova, M. & Dimitrov, D. Liposome electroformation. *Faraday Discussions* **81**, 303-311 (1986).

66. Ruiz-Taylor, L. *et al.* Monolayers of derivatized poly(L-lysine)-grafted poly(ethylene glycol) on metal oxides as a class of biomolecular interfaces. *Proceedings of the National Academy of Sciences of the United States of America* **98**, 852-857 (2001).

67. Stamou, D., Duschl, C., Delamarche, E. & Vogel, H. Self-assembled microarrays of attoliter molecular vessels. *Angewandte Chemie-International Edition* **42**, 5580-5583 (2003).

68. Kunding, A., Mortensen, M., Christensen, S. & Stamou, D. A fluorescence-based technique to construct size distributions from single-object measurements: Application to the extrusion of lipid vesicles. *Biophysical Journal* **95**, 1176-1188 (2008).

69. Hatzakis, N. *et al.* How curved membranes recruit amphipathic helices and protein anchoring motifs. *Nature Chemical Biology* **5**, 835-841 (2009).

70. Aguet, F., Antonescu, C., Mettlen, M., Schmid, S. & Danuser, G. Advances in Analysis of Low Signal-to-Noise Images Link Dynamin and AP2 to the Functions of an Endocytic Checkpoint. *Developmental Cell* **26**, 279-291 (2013).